Research Square

Preprints are preliminary reports that have not undergone peer review.
They should not be considered conclusive, used to inform clinical practice,
or referenced by the media as validated information.

Mapping the Stemness Landscape of Glioblastoma to Drive Heterogeneity and Drug Resistance: Bridging Pathological Omics with Prognostic Outcomes

Yifan Xu
Department of Neurosurgery, The Affiliated Hospital of Qingdao University, Qingdao City, 266000, China
Jinpeng Wu
Department of Neurosurgery, The Affiliated Hospital of Qingdao University, Qingdao City, 266000, China
Junshan Wan
Department of Neurosurgery, The Affiliated Hospital of Qingdao University, Qingdao City, 266000, China
Zhongxiang Guo
Department of Neurosurgery, The Affiliated Hospital of Qingdao University, Qingdao City, 266000, China
Huanting Li
Department of Neurosurgery, The Affiliated Hospital of Qingdao University, Qingdao City, 266000, China
Shifang Li
Department of Neurosurgery, The Affiliated Hospital of Qingdao University, Qingdao City, 266000, China
Shihao He
Johns Hopkins School of Medicine
yugong Feng
Department of Neurosurgery, The Affiliated Hospital of Qingdao University, Qingdao City, 266000, China
Pin Guo
guopin116@qdu.edu.cn

Department of Neurosurgery, The Affiliated Hospital of Qingdao University, Qingdao City, 266000, China

Research Article

Keywords: Glioblastoma, scRNA-seq, glioblastoma stem cells, tumor microenvironment, ResNet-50

Posted Date: August 20th, 2026

DOI: https://doi.org/10.21203/rs.3.rs-9815299/v1

License: This work is licensed under a Creative Commons Attribution 4.0 International License.
Read Full License

Additional Declarations: No competing interests reported.

Mapping the Stemness Landscape of Glioblastoma to Drive Heterogeneity and Drug Resistance: Bridging Pathological Omics with Prognostic Outcomes

Yifan Xu[1†], Jinpeng Wu[1†], Junshan Wan[1†], Zhongxiang Guo[1], Huanting Li[1], Shifang Li[1], Shihao He[2], Yugong Feng[1*], Pin Guo[1*].*

[1]Department of Neurosurgery, The Affiliated Hospital of Qingdao University, Qingdao City, 266000, China.

[2]Department of Pathology, Johns Hopkins School of Medicine, Baltimore, Maryland, 21205, USA.

†These authors have contributed equally to this work and share the first authorship

** Corresponding author:*

Pin Guo M.D.

Department of Neurosurgery, The Affiliated Hospital of Qingdao University, Qingdao, 266000, China. e-mail: guopin116@qdu.edu.cn

Yugong Feng M.D.

Department of Neurosurgery, The Affiliated Hospital of Qingdao University, Qingdao, 266000, China. e-mail: fengyugong@qdu.edu.cn

Shihao He M.D.

Department of Pathology, Johns Hopkins School of Medicine, Baltimore, Maryland, 21205, USA. e-mail: Heshihaoo@outlook.com

Abstract

Background: Glioblastoma (GBM) exhibits profound cellular heterogeneity and therapeutic resistance, largely driven by glioblastoma stem cells (GSC), yet their spatial dynamics and regulatory mechanisms remain incompletely understood.

Methods: We integrated large-scale single-cell and spatial transcriptomic datasets encompassing over 338,000 cells, combined with computational pathology and machine learning to delineate stemness landscapes and construct prognostic models.

Results: Three stemness-defined subpopulations were identified, revealing a dynamic differentiation continuum and extensive intercellular communication networks. GSC displayed enhanced signaling activity, metabolic reprogramming, and immunosuppressive microenvironmental interactions. A robust prognostic model stratified patients into distinct risk groups with differential immune infiltration and therapeutic sensitivity. TUBB2B was identified as a key regulator of stemness and experimentally validated, with its inhibition synergizing with temozolomide.

Conclusions: This study provides a comprehensive multi-omics framework linking stemness heterogeneity to prognosis and therapy in GBM, highlighting TUBB2B as a promising therapeutic target and offering insights for precision oncology.

Keywords

Glioblastoma, scRNA-seq, glioblastoma stem cells, tumor microenvironment, ResNet-50

1.Introduction

GBM is the most aggressive and prevalent type of primary malignant brain tumor, accounting for approximately 50% of all glioma cases[1,2]. Despite the implementation of intensive treatment strategies, including surgical resection, radiotherapy, and chemotherapy, the clinical prognosis remains dismal, with a median survival time seldom exceeding 15 months and a five-year survival rate below 5%[3,4]. The substantial genomic instability, extensive cellular heterogeneity, complex TME, and the development of treatment resistance mechanisms collectively represent the key challenges underlying the high failure rate of current GBM therapies[3,5,6].

The adaptability of GBM to current therapies is largely due to its complex molecular and pathological characteristics[7]. These features include a diverse cellular composition, such as tumor-initiating stem cells, mechanisms of immune evasion, and a highly vascularized stroma, the heterogeneity of which complicates therapeutic targeting[8,9]. Moreover, GBM cells frequently exhibit genetic alterations, including mutations in the epidermal growth factor receptor and tumor suppressor genes such as

TP53 and PTEN, contributing to their invasive nature and resistance to treatment[10,11]. GSC are a subset of GBM cells characterized by their capacity for self-renewal and multi-lineage differentiation[12,13]. These properties contribute to their role as key drivers of radiation resistance and are closely associated with poor clinical prognosis[14]. GSC exhibit sustained proliferative potential, the ability to differentiate into multiple cell lineages, and strong tumorigenicity in vivo[15], making them central mediators of GBM recurrence and therapeutic resistance[16]. The identification of novel markers and molecular mechanisms underlying GSC maintenance may offer a promising approach for developing more effective GBM treatment strategies.

The scRNA-seq and spatial stRNA-seq technologies have provided unprecedented resolution in elucidating tumor cell heterogeneity and the TME[17]. These approaches have not only enabled the identification of cell subpopulations exhibiting stem cell-like properties and therapeutic resistance[18,19], but also characterized the dynamic interactions among immune cells, stromal cells, and tumor cells, thereby establishing a foundation for investigating the mechanisms underlying tumor progression and immune evasion[20]. Currently, traditional biopsy-based histopathological examination often fails to fully capture the heterogeneity and complexity of tumor characteristics. However, recent advancements in computational pathology offer unprecedented opportunities to enhance our understanding of the TME in GBM and the molecular mechanisms underlying its heterogeneity[21]. Computational pathology presents a promising approach to bridge the gap between conventional histological analysis and contemporary molecular insights[22]. By leveraging digital pathology, high-throughput sequencing, and machine learning algorithms, researchers are now capable of quantitatively analyzing the histological features of tissue slides with exceptional precision[23]. This enables detailed examination of cellular morphology, structural arrangement, and pathological changes to accurately determine the nature, stage, and classification of diseases[24]. Furthermore, the integration of multi-omics data has provided valuable insights into the complex molecular signaling pathways involved in GBM, leading to the

identification of biomarkers associated with GBM progression and treatment response.

In this study, we systematically analyzed scRNA-seq and stRNA-seq datasets to develop and validate GSC features, and investigated the underlying mechanisms of GSC involvement in tumor microenvironment heterogeneity, intercellular communication, and tumor progression. Subsequently, a robust prognostic model was constructed using machine learning algorithms. Furthermore, we identified TUBB2B as a key regulatory target in the initiation and progression of GSC and validated our findings through experimental approaches. This research not only addresses a current gap in the integrated application of multi-omics and computational pathology in GBM, but also offers novel insights for future studies on glioma stem cell-driven drug resistance mechanisms. The flowchart of this study is shown in **Figure 1**.

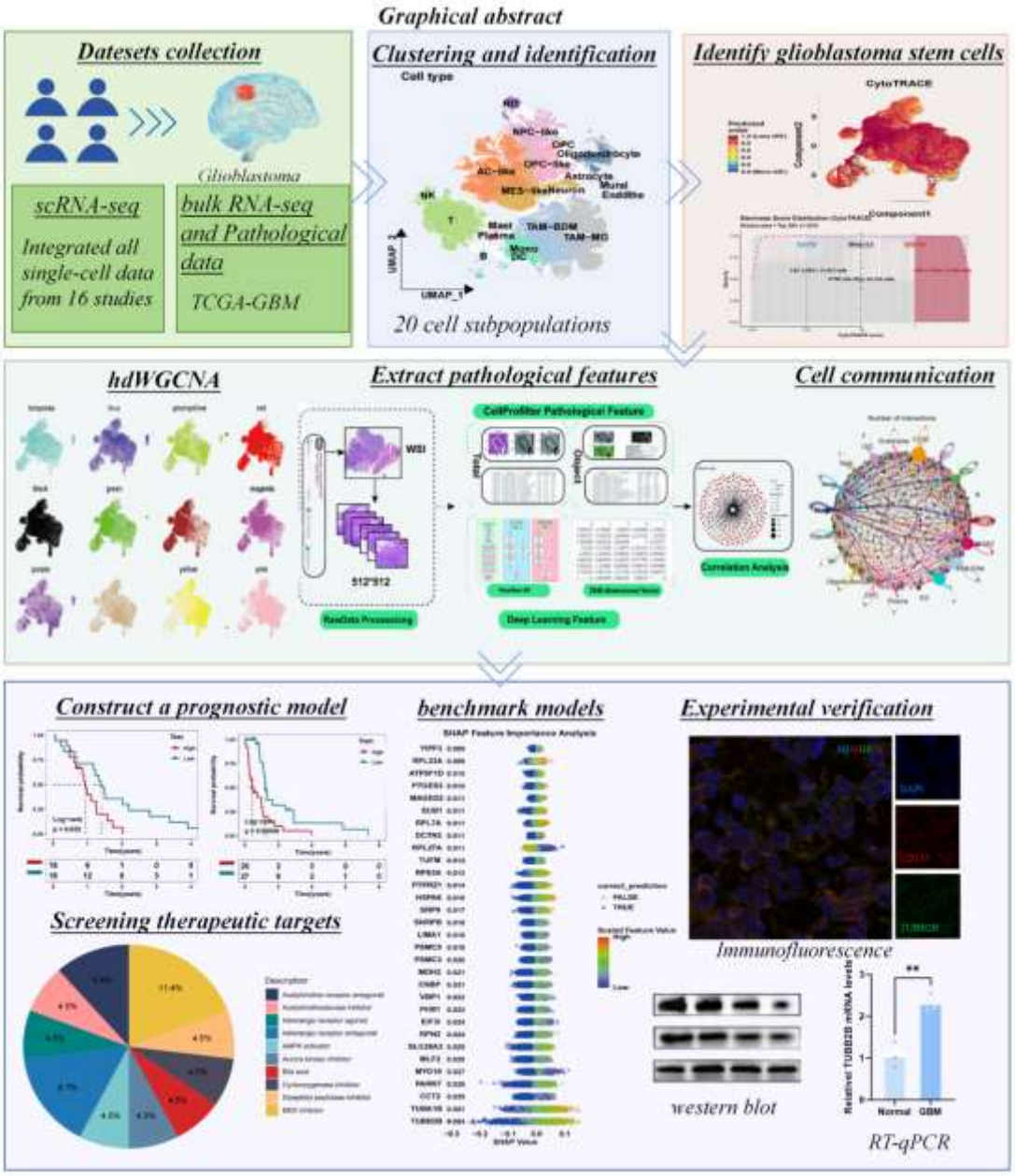


Figure 1. Flowchart of the process mechanism of this study.

2.Results

2.1 Identify glioblastoma stem cells through single-cell atlas

To establish a high-quality core reference for the GBM genome, we compiled scRNA-seq data generated from multiple platforms and diverse sample preparation protocols across 16 independent studies, encompassing more than 338,564 cells derived from 109 patients (**Figure 2A-B**). In the initial analysis phase, we employed a curated list of cell-type-specific markers for automated cell annotation and

supplemented this with unsupervised manual classification. This integrated approach enabled us to categorize a broad spectrum of cell types into 20 distinct subpopulations: AC-like, Astrocyte, B cell, CD4/CD8 T cell, DC, Endothelial cell, MES-like, Mast cell, Monocyte, Mural cell, NK cell, NPC-like, Neuron, OPC, OPC-like, Oligodendrocyte, Plasma B cell, RG, TAM-BDM and TAM-MG (**Figure 2C, Supplementary Table 1**). **Figures 2D-G** present UMAP dimensionality reduction plots for multiple cell marker genes across various cell populations, illustrating the density distribution of gene expression levels. We conducted a large-scale CytoTRACE analysis on 127,521 tumor cells (**Figure 2H**), which revealed the heterogeneity of stemness potential across the tumor landscape. This computational framework utilizes gene expression counts as a reliable surrogate for cellular differentiation status and demonstrates higher resolution in capturing cellular plasticity compared to conventional stem cell markers. Subsequently, by applying a stringent interquartile range classification method (75th and 25th percentiles) to all tumor cells, we identified three distinct cell states (**Figure 2I**): glioblastoma stem cells (GSC, n = 31,777), which exhibit high CytoTRACE scores and align with the cancer stem cell paradigm, displaying molecular features similar to neural progenitor cells; dynamic transition stem cells (DTSC, n = 63,872), a moderately scored population showing partial differentiation markers, potentially representing transitional states during tumor progression; and low stemness cells (LSC, n = 31,872), the predominant low-scoring group, exhibiting terminal differentiation patterns while retaining some degree of cellular plasticity. To further evaluate whether the CytoTRACE-based stratification corresponded to established stemness-associated programs, we examined canonical stem cell markers and transcriptional signatures. PROM1 (CD133), a widely recognized neural stem cell–associated marker, showed preferential expression within the CytoTRACE-high population (**Figure S1A**). Co-localization analysis demonstrated a positive association between PROM1 expression and CytoTRACE scores at the single-cell level (**Figure S1B, C**), supporting concordance between transcriptional complexity modeling and established stemness markers. Importantly, the CytoTRACE-high group also exhibited

coordinated upregulation of stemness-related gene programs (**Figure S1D**), suggesting enrichment of plasticity-associated transcriptional networks rather than isolated proliferative signals. The UMAP visualization revealed clear spatial separation among the stem cell subpopulations (**Figure 2J-K**), with GSC occupying distinct regions within the manifold structure. Density gradient analysis indicated a GSC-enriched microenvironment, suggesting that the tumor microenvironment may regulate stemness. Pseudotime reconstruction (**Figure 2L**) illustrated a unidirectional developmental trajectory from GSC to LSC. Furthermore, Ro/e analysis was employed to evaluate the anatomical distribution of the identified cell subpopulations. This analysis quantified the relative abundance of GSC, LSC, and DTSC across different anatomical regions (**Figure 2M-N**), revealing significant enrichment of GSC within the OPC-like subpopulation.

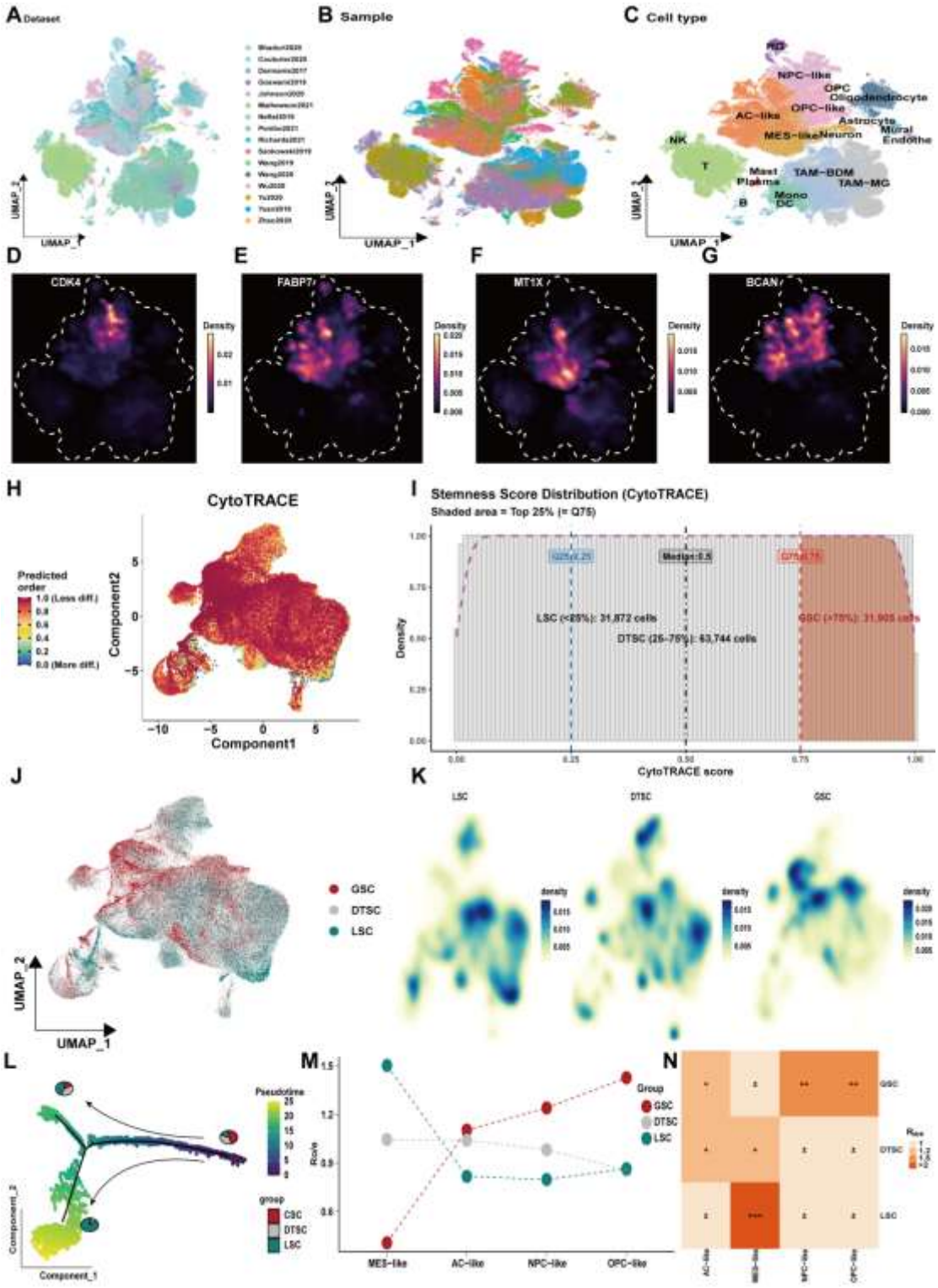


Figure 2. Mapping the single-cell atlas of GBM and identification of GSC subpopulations. **(A)** A single-cell atlas was drawn by integrating 338,564 cells from 16 studies. **(B)** Generate single-cell maps for each sample. **(C)** The UMAP plot shows that 20 cell subpopulations were identified. **(D-G)** UMAP visualization highlights the expression patterns of representative marker genes for each cell type. **(H-I)** Cytotrace

evaluates the stemness of cells. Based on the IQR, cells are categorized into three distinct groups: GSC. **(J-K)** The UMAP plot illustrates the spatial distribution patterns of these three cell groups. **(L)** Pseudotime trajectory analysis demonstrates the progressive transition from GSC to the LSC state, emphasizing the gradual alterations in genomic instability throughout the process of cell differentiation. **(M-N)** A Ro/e analysis of the enrichment of three groups of cells in different cell subpopulations.

2.2 Inter-cellular communication and heterogeneity analysis among all cell types

The intercellular communication analysis reflects the frequency and intensity of interactions among GSC, DTSC, LSC and other cell types (**Figure 3A**). Research findings on cell communication demonstrate that GSC exhibit an increased propensity to transmit signaling molecules, particularly through the pleiotrophin (PTN) and midkine (MK) pathways. “PTN and MK pathways” refer to pleiotrophin-and midkine-mediated ligand-receptor signaling pathways involved in cell-cell communication, rather than canonical intracellular signaling cascades. Furthermore, their capacity to receive signals via the EGF and TWEAK pathways is also enhanced (**Figure 3B**). The GSC subpopulation depicted on the surface in **Figure 3C** exhibits a stronger capacity for signal transduction. Furthermore, the overall level of intercellular communication across the three groups demonstrates a progressively increasing trend. Quantitative comparisons reveal that GSC, functioning concurrently as both signal senders and receivers, engage in significantly more ligand-receptor interactions with various cell types, particularly mural cells, astrocytes, and OPC (**Figure 3D-E**). Pathway clustering further indicates that GSC are associated with the activation of MAPK, EGFR, and Androgen signaling pathways, whereas LSC may be closely linked to the PI3K pathway, suggesting potential tumor-suppressive characteristics (**Figure 3F**). The detailed ligand-receptor analysis indicates that multiple signaling pathways, such as the pleiotropic protein-nucleolar protein (PTN-NCL), exhibit a higher expression level in GSC compared to other cell types,

but not a solely increased expression state. (**Figure 3G**). **Figure 3H** evaluates the sensitivity of GSC to various drugs. Based on standardized drug response data, statistically significant differences were identified, and drugs showing distinct sensitivity or resistance were selected. CAPSAICIN (sig-20625), F1061-0156 and CAPSAICIN (Sig-7082) were identified as highly sensitive drugs, with CAPSAICIN exhibiting significant resistance or reactivity specifically within the GSC population. Finally, through the enrichment analysis of metabolic pathways using scMetabolism25, the results demonstrated that GSC exhibited significant upregulation compared to DTSC and LSC in several metabolism-related pathways, including histidine metabolism, inositol phosphate metabolism, and linoleic acid metabolism. This suggests that GSC may involve multiple potential pathogenic mechanisms associated with metabolic reprogramming (**Figure 3I**).

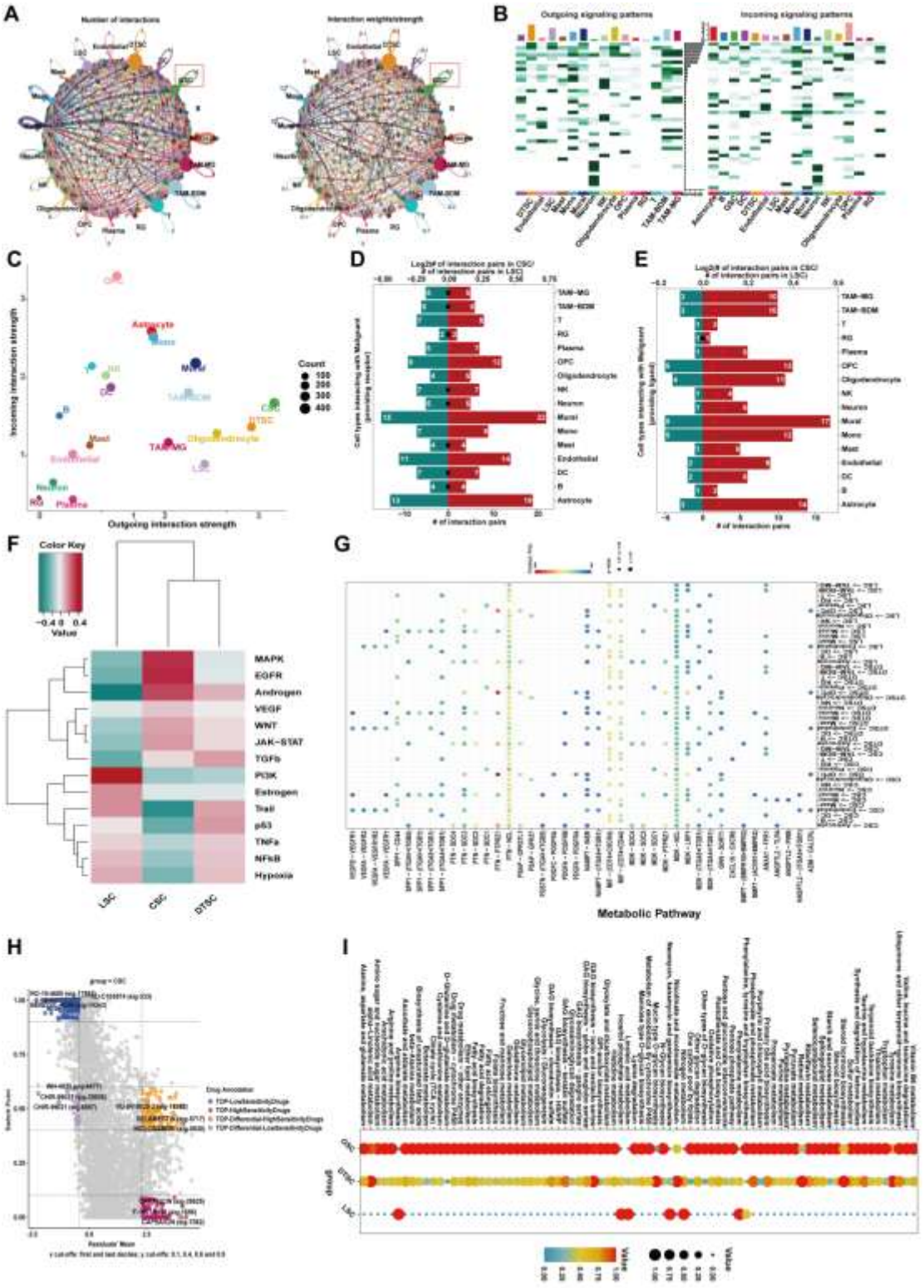


Figure 3. Inter-cellular communication of GSC and enriched metabolic pathways. **(A)** The intercellular interaction network illustrates the number (left panel) and strength (right panel) of interactions among GSC, DTSC, LSC and other cell types. **(B)** The interaction quantity and weight/strength of cellular interactions within the

communication network of GBM. **(C)** Scatter plots depicting the interaction strength between outgoing and incoming within each cell subpopulation indicate that GSC exhibit the highest outgoing interaction strength. **(D-E)** The ligand-receptor interaction levels between GSC and LSC, as well as those involving other cell types, were quantified. **(F)** Pathway enrichment analysis of GSC, DTSC and LSC. **(G)** Bubble chart depicting selected ligand-receptor pairs enriched in GSC, DTSC, LSC and other cell types. **(H)** Drug sensitivity analysis of GSC. **(I)** The metabolic pathway enrichment analysis of GSC, DTSC and LSC revealed that GSC exhibited significant upregulation across all metabolic pathways.

2.3 HdWGCNA revealed the genes related to the GSC modules

This study employed the hdWGCNA method, aiming to identify the gene modules with high degree of stemness. The optimal soft threshold power was determined through a function. The power of 10 raised to a certain exponent was selected to represent the minimum value that the network could satisfy the scale-free topological condition (the scale-free topological fitting index R2 > 0.8) while maintaining sufficient average connectivity. (**Figure 4A**), a scale-free co-expression network was constructed, leading to the identification of 12 distinct modules (**Figure 4B**). Among these, the magenta, green, red, blue, and turquoise modules exhibited high activation levels in the GSC group (**Figure 4C, Supplementary Table S2**). The UMAP visualization illustratedthe distribution patterns of cell subpopulations within each module (**Figure 4D**). After the network is constructed, the membership of module members is evaluated using the connectivity based on characteristic genes (kME). Genes with a kME value of $\geqslant$ 0.3 are retained to ensure a moderate to strong association with the corresponding module, thereby reducing the noise-driven gene-module assignment. A total of 238 GSC-related genes were finally selected. (**Figure 4C, Supplementary Table S3**). Subsequently, we assessed the inter-module correlations(**Figure 4E**). To investigate the prevalence and clinical relevance of the GSC genesignature in GBM, we validated its expression using TCGA-GBM dataset. The results revealed that GSC activity in GBM tissues was significantly elevated

compared to normal brain tissues (**Figure 4F**).

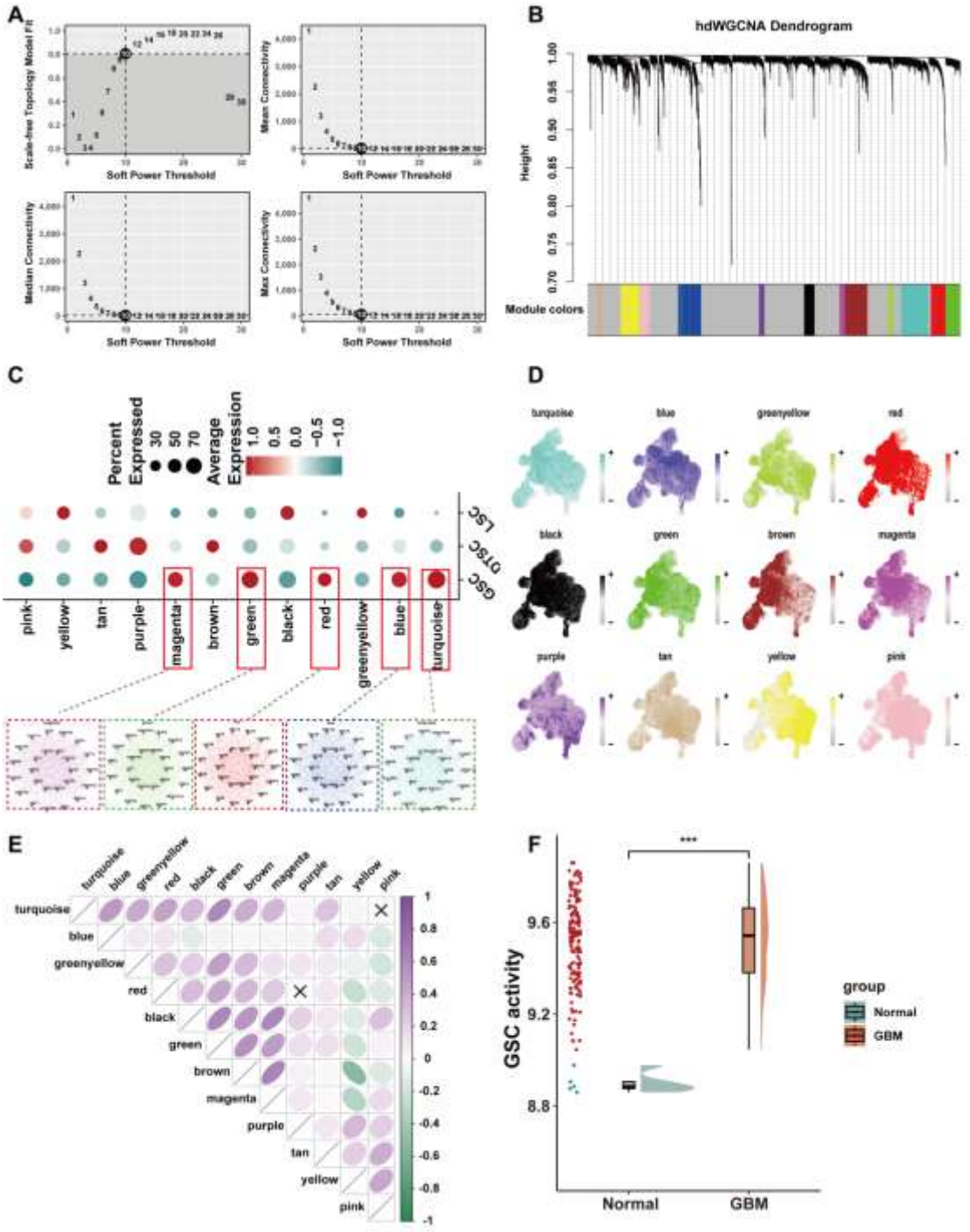


Figure 4. The hdWGCNA analysis identified the magenta, green, red, blue, and turquoise modules as the five core modules significantly correlated with the GSC group. (**A**) A scale-free network was constructed using a soft thresholding power of 10. (**B**) The 12 gene modules within this network were visualized using a dendrogram. (**C**) Differential expression levels of each gene module were assessed across the GSC,

DTSC, and LSC groups. (**D**) The distribution patterns of these 12 gene modules were analyzed specifically within the GSC group. (**E**) Correlation analysis was conducted among the 12 gene modules. (**F**) GSC activity was validated in both GBM tissues and normal brain tissues.

2.4 Spatial transcriptome analysis reveals the spatial distribution and expression intensity of cell subpopulations.

H&E staining of tissue sections illustrated the overall morphology of the samples, providing a comprehensive overview of the spatial architecture, with a specific focus on differentiating distinct tissue regions (**Figure 5A**). Subsequently, we scored and projected GSC-associated gene sets onto spatial transcriptomics data, visualizing their spatial distribution across the entire tissue section. This distribution is represented by a color gradient ranging from 1 (low score) to 4 (high score), reflecting the relative enrichment of GSC-associated transcriptional programs in different spatial regions (**Figure 5B**). This approach characterizes the spatial heterogeneity of stemness-related transcriptional signals within the tissue. Cell types were classified using SPOTlight analysis, with each point colored according to its predicted cell type. Cells were categorized into six groups, generating a spatial representation of these cell types and highlighting their complex spatial organization throughout the sample (**Figure 5C**). Subsequently, a correlation heatmap was generated for each cell type within the clusters, illustrating the degree of overlap and correlation among their gene expression profiles (**Figure 5D**). Network analysis diagram revealed the functional relationships and interactions between different cell types based on the expression of marker genes (**Figure 5E**). Violin plots displayed the stemness scores for the identified cell types, encompassing metrics such as AUCell, UCell, singscore, ssGSEA, and Add, thereby quantifying their stem-like characteristics (**Figure 5F**).

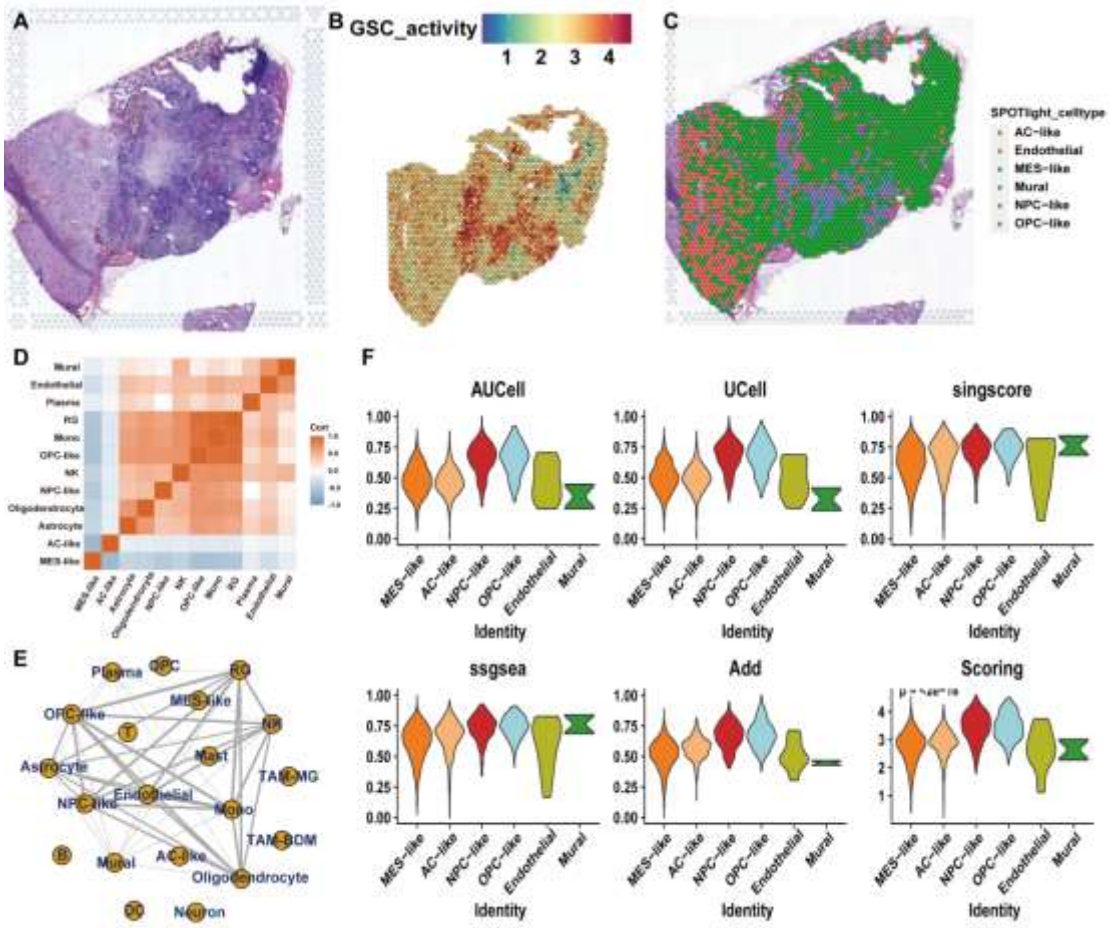


Figure 5. Spatial transcriptome analysis assesses the spatial distribution of cell stemness. (A) H&E staining revealed clearly defined histological regions within the stRNA samples. (B) A spatially resolved metabolic map of GSC. (C) GBM tissue architecture inferred through unsupervised clustering analysis.

2.5 Pathological features and deep learning features were extracted to construct a prognostic model for GBM.

We utilized a large cohort of 358 samples for pathological omics analysis, each accompanied by histopathological slides and whole-exome sequencing data. WSIs from the TCGA-GBM dataset were accurately segmented into image patches, and pathological features were extracted using CellProfiler, while deep learning features were extracted using the ResNet-50 model (**Figure 6A**). This dual strategy yielded 617 morphological features via CellProfiler and 2048 deep learning features via ResNet-50. Gene set variation analysis (GSVA) was performed on a set of 238 genes associated with high stemness within the TCGA-GBM cohort. To investigate the

association between these pathological clustering features and GSC, Spearman's correlation analysis was conducted, revealing 220 significantly correlated features ($P<0.05$), including 38 morphological features derived from CellProfiler (**Supplementary Table S4**) and 182 deep learning features extracted by the ResNet-50 model (**Supplementary Table S5**). These stemness-associated pathological features were then integrated into machine learning models to construct a prognostic framework for GBM. A preliminary univariate regression analysis was carried out on the 220 pathological features, leading to the selection of 6 hub features for model development (**Figure 6C, Supplementary Table S6**). Seven machine learning algorithms related to survival analysis—Elastic Net (Enet), Lasso regression, Ridge regression, XGBoost, plsRcox, SuperPC, and CoxBoost—were assessed to identify the model with the highest predictive accuracy and the lowest risk of overfitting. To validate performance and optimize hyperparameters, a nested cross-validation approach was employed using the TCGA-GBM dataset, consisting of 10 outer folds and 5 inner folds (**Figure 6B**). The performance of the models was evaluated using the concordance index (C-index) and the integrated Brier score (IBS). Among all models evaluated, Ridge regression consistently achieved the highest C-index and the lowest IBS, indicating superior predictive performance and robustness. Therefore, Ridge regression was selected as the optimal survival prediction model (**Figure 6D-E**). To evaluate the clinical utility of the model, individual risk scores were calculated for each patient, and patients were stratified into high-risk and low-risk groups based on the median risk score. Kaplan-Meier survival analysis demonstrated a statistically significant difference in overall survival between the two groups, with high-risk patients exhibiting significantly poorer survival outcomes in both the training and validation cohorts (**Figure 6F-G**). Furthermore, ROC curve analysis was conducted to assess the model's predictive performance. In the training cohort, the AUC values for predicting 1-year, 2-year, and 3-year overall survival were 0.81, 0.78, and 0.78, respectively (**Figure 6H**). In the validation cohort, the corresponding AUC values were 0.65, 0.72, and 0.72, respectively (**Figure 6I**), suggesting consistent prognostic accuracy of the model

across different time points.

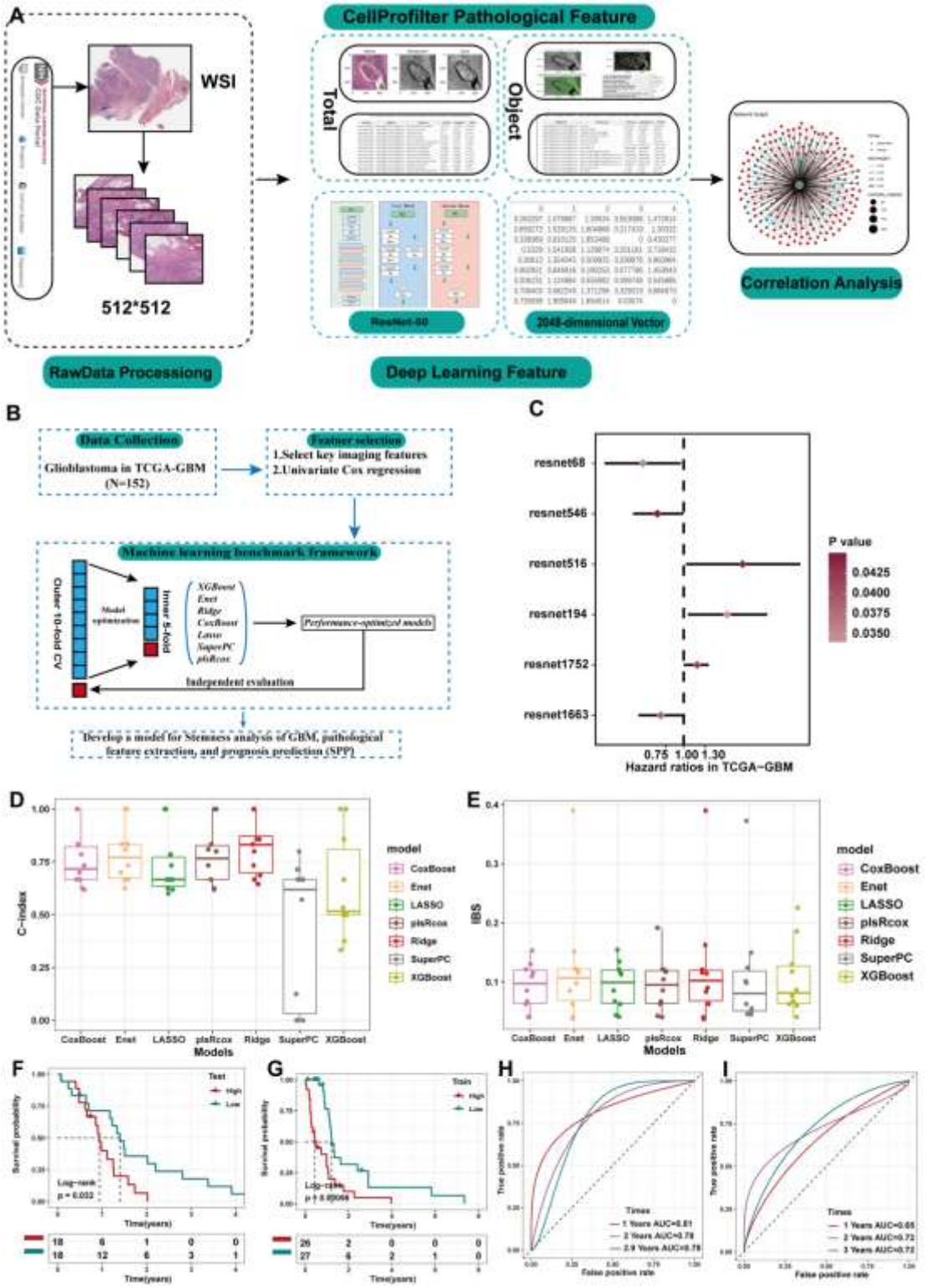


Figure 6. A comprehensive prognostic model for glioblastoma integrating pathological and deep learning features. (**A**) Flowchart illustrating the feature

extraction process using CellProfiler and the ResNet-50 model. (**B**) Schematic representation of the nested cross-validation framework applied across seven survival analysis algorithms. (**C**) Univariate regression analysis identified six key prognostic features associated with GBM. (**D-E**) Comparative evaluation of model performance using C-index and integrated Brier score (IBS) metrics. (**F-G**) Kaplan-Meier survival curves stratifying patients into high-risk and low-risk groups. (**H-I**) ROC curves assessing the model's predictive accuracy for 1-year, 2-year, and 3-year overall survival outcomes.

2.6 Characterization of the immune microenvironment in high riskscore and low riskscore GBM patients

The immune microenvironment constitutes a critical component of the TME. Tumor cells can evade immune surveillance through various mechanisms, such as the interaction of immune checkpoint molecules (e.g., PD-L1, CTLA-4) with their corresponding receptors on immune cells, which subsequently inhibits immune cell activation and function. The immune microenvironment in GBM is typically characterized by a highly immunosuppressive state. Based on the extent of immune cell infiltration and functional activity, tumors can be broadly categorized into "hot tumors" and "cold tumors". Hot tumors are generally associated with substantial infiltration of activated immune cells, whereas cold tumors exhibit limited immune cell infiltration and reduced immune activity, often in the presence of a robust immunosuppressive microenvironment. Therefore, we conducted further investigations to comprehensively analyze the association between patient prognosis scores and immune regulatory features. In the low riskscore group, a significant increase in the infiltration of T cells, CD8+ T cells, NK cells, and macrophages was observed. These findings suggest that patients with lower riskscore may harbor immunologically "hot" tumors, while those with higher riskscore may present with immunologically "cold" tumors (**Figure 7A**). Histopathological analysis further supported this observation, demonstrating a strong negative correlation between prognosis score and the degree of immune infiltration (**Figure 7B**).

2.7 Screening potential therapeutic targets and candidate drugs for high riskscore patients

We further conducted an in-depth analysis of the biological characteristics of patients in the high-risk score group. Pathway enrichment analysis based on gene expression profiles revealed that pathways associated with stemness were significantly enriched in the high-risk group (**Figure 7C**), which aligns with our research findings. Additionally, SubMap analysis was employed to evaluate the potential influence of the TME on immunotherapy responsiveness. The results suggest that patients in the low-risk group may exhibit greater responsiveness to PD-1 and CTLA4-based immunotherapies (**Figure 7D**). In the sensitivity analysis of targeted therapeutic agents, we observed that the half-maximal inhibitory concentration (IC50) of AZD6244 was lower in the high-risk group, indicating a potentially higher therapeutic benefit of this agent in patients with a high-risk score (**Figure 7E**). To identify candidate effective compounds, we conducted a Connectivity Map (CMap) analysis. Initially, differential gene expression analysis was performed to identify gene expression differences between the high- and low-risk score groups. First, we performed a differential gene expression analysis to investigate the differences in gene expression between the high-risk and low-risk score groups. Subsequently, we selected the top 150 upregulated and 150 downregulated genes as features for the prognostic score and calculated their corresponding CMap scores. Using this method, we identified a total of 105 compounds with CMap scores lower than -50 (**Supplementary Table 7**). Among these compounds, 11.4% were classified as MEK inhibitors, and 9.1% were other targeted therapeutic agents (**Figure 7F**). Finally, we further explored potential sensitive drugs through a comprehensive analytical process (**Figure 7G**). Specifically, four compounds (Birinapant, Dasatinib, PD318088, Selumetinib) were selected from the CTRP database, and four additional compounds (AZS8330, AZD8931, TAK-733, Trametinib) were selected from the PRISM database (**Figure 7H**). The AUC values of these compounds were significantly negatively correlated with the risk score and exhibited significantly lower values in the high-risk

group, indicating that these drugs may offer greater therapeutic potential for patients in the high-risk category.

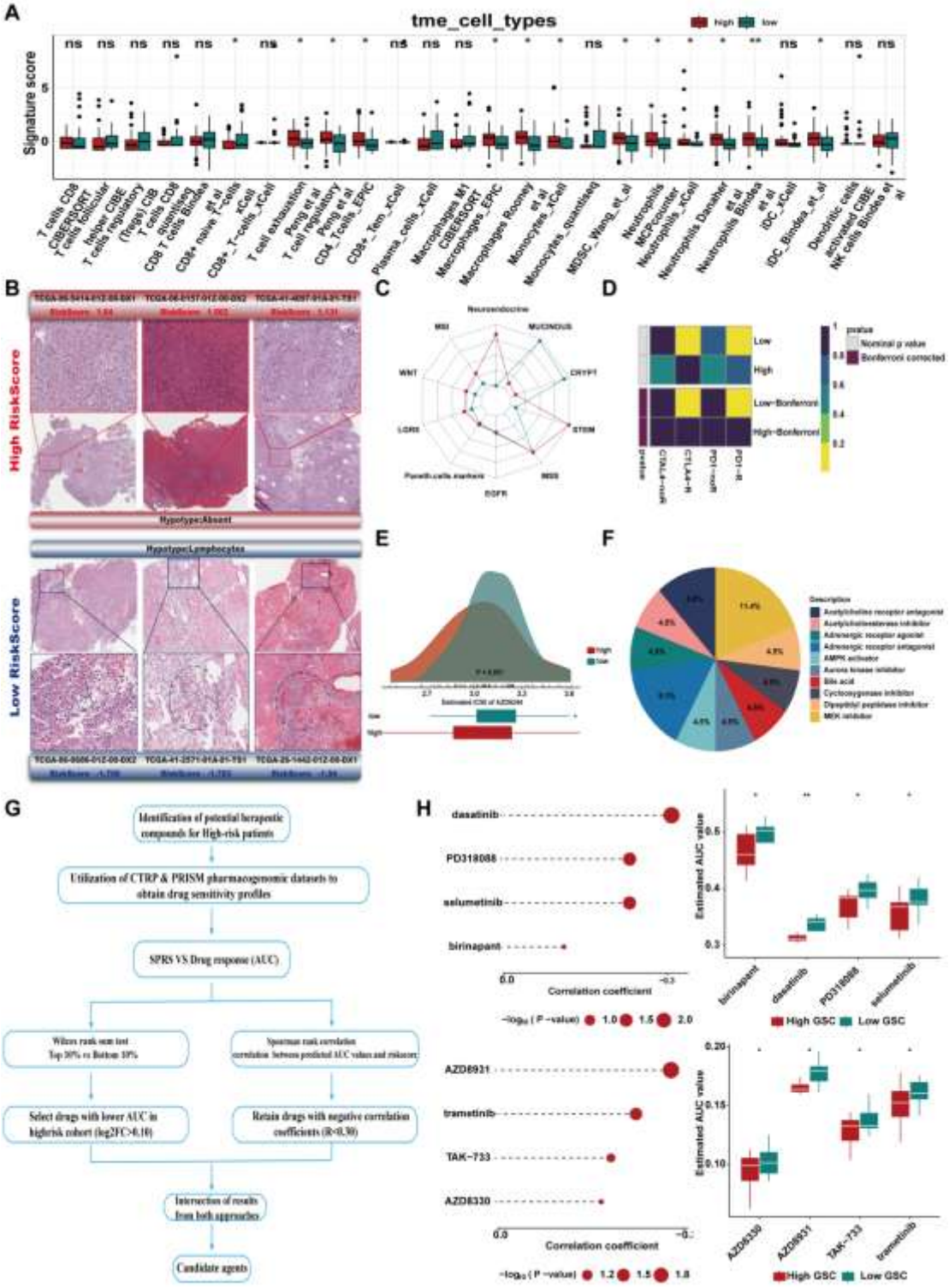


Figure 7. Characterization of the immune microenvironment and identification of potential therapeutic agents in high-risk and low-risk GBM patients. (**A**) Box plots

depicting the distribution of immune cell characteristics in high-risk and low-risk groups. (**B**) Representative histological images illustrating variations in immune cell infiltration between high-risk (upper panel) and low-risk (lower panel) patients. (**C**) Pathway enrichment analysis reveals that stemness-associated pathways are significantly enriched in the high-risk cohort. (**D**) Assessment of the influence of the TME on immunotherapy response. (**E**) IC50 analysis of targeted therapeutic agents demonstrates a significantly reduced IC50 value for AZD6244 in the high-risk group, suggesting that high-risk patients may derive greater therapeutic benefit from this treatment. (**F**) Distribution of drug categories identified through CMap analysis. (**G**) Summary of the drug screening workflow. (**H**) Scatter plots and box plots illustrating the correlation between drug AUC values and the risk score. (ns, not significant, *P < 0.05, **P < 0.01).

2.8 Machine learning prediction models and benchmark models for identifying characteristic genes related to GSC

After ranking GSC-related genes using the random forest algorithm, we selected the top 100 genes with the highest importance scores (**Supplementary Table S8**). The ABESS method was subsequently employed to refine the feature set, resulting in a final model comprising 31 genes that demonstrated optimal predictive performance (**Figure 8A–C, Supplementary Table S9**). To evaluate the predictive capability of different machine learning approaches for identifying the high stemness phenotype in GBM, we implemented multiple classification algorithms, including LDA, KKNN, GLM, Naive Bayes, Random Forest, Rpart, and XGBoost (**Figure 8D**). The results indicated that the random forest model outperformed other classifiers in terms of AUC, highlighting its superior capacity to manage complex gene expression patterns and nonlinear relationships, as well as demonstrating strong stability and generalization. In the independent validation cohort, the model achieved near-perfect accuracy, further supporting its clinical reliability and applicability (**Figure 8E–G**). Decision curve analysis confirmed that the model offers substantial net clinical benefits across various risk thresholds and surpasses conventional all-positive or all-negative

strategies in guiding personalized treatment decisions. From an interpretability perspective, SHAP values illustrated the contribution of each gene to the model's predictions, emphasizing the pivotal role of TUBB2B in distinguishing GSC identity (**Figure 8H**), thereby underscoring the potential of machine learning in identifying tumor stemness features.

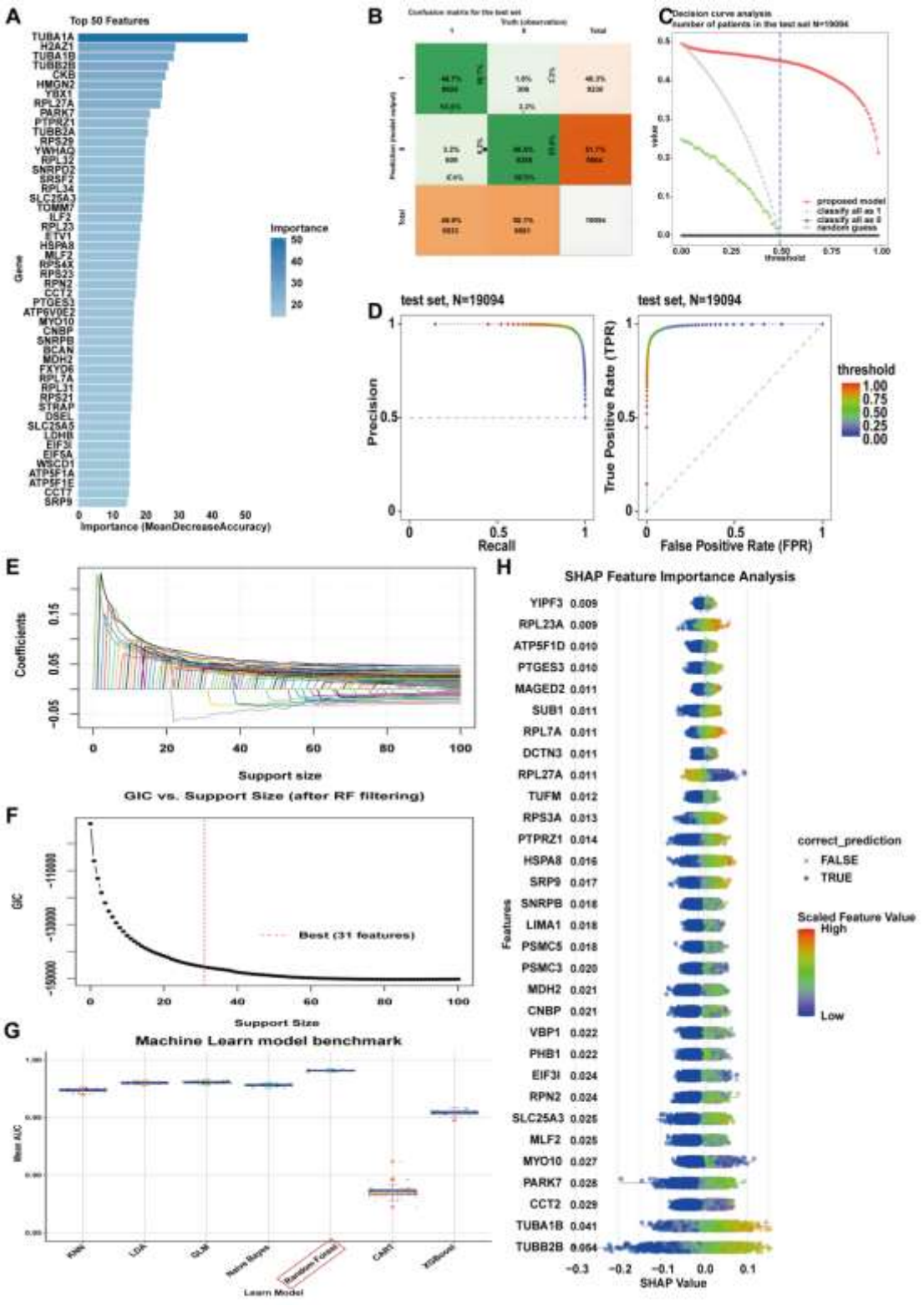


Figure 8. Identification of hub GSC-Related genes using machine learning approaches. (**A**) Top 100 GSC-associated genes ranked by their importance scores derived from the random forest algorithm. (**B–C**) Performance metrics of the optimized 31-gene random forest classification model. (**D**) Comparative assessment

of seven classification algorithms demonstrates that the random forest model attains the highest AUC value. (**E**) Confusion matrix illustrating classification accuracy. (**F**) Decision curve analysis for evaluating clinical utility. (**G**) Performance evaluation of the random forest model on an independent validation dataset. (**H**) SHAP value analysis for enhanced model interpretability.

2.9 TUBB2B serves as a critical target for regulating the stemness of GSC

The WB (**Figure 9A-B**) and qRT-PCR (**Figure 9C**) demonstrated that the expression level of TUBB2B in GBM tissues was significantly elevated compared to that in normal brain tissues. Subsequently, in the GSC derived from the GBM, both CD133 and TUBB2B showed high expression levels (**Figure 9D-F**). The IHC results further corroborated this observation (**Figure 9G-H**). Furthermore, IF staining for GSC markers, including CD133 and TUBB2B, performed on the tissue microarray revealed a significant upregulation of TUBB2B in glioblastoma tissues, which was accompanied by elevated expression of CD133 (**Figure 9I-J**). In established GBM cell lines (U87MG, U251, and T98G), GSC-like populations were defined as CD133-positive cells isolated by magnetic bead sorting and subsequently cultured under stem cell-promoting conditions. These enriched CD133+ fractions exhibited elevated expression of canonical stem cell markers, including CD133 and OLIG2, confirming successful enrichment of stem-like subpopulations. Within these GSC-enriched populations, TUBB2B expression was significantly upregulated compared with unsorted parental cells (**Figure 9K-M**).

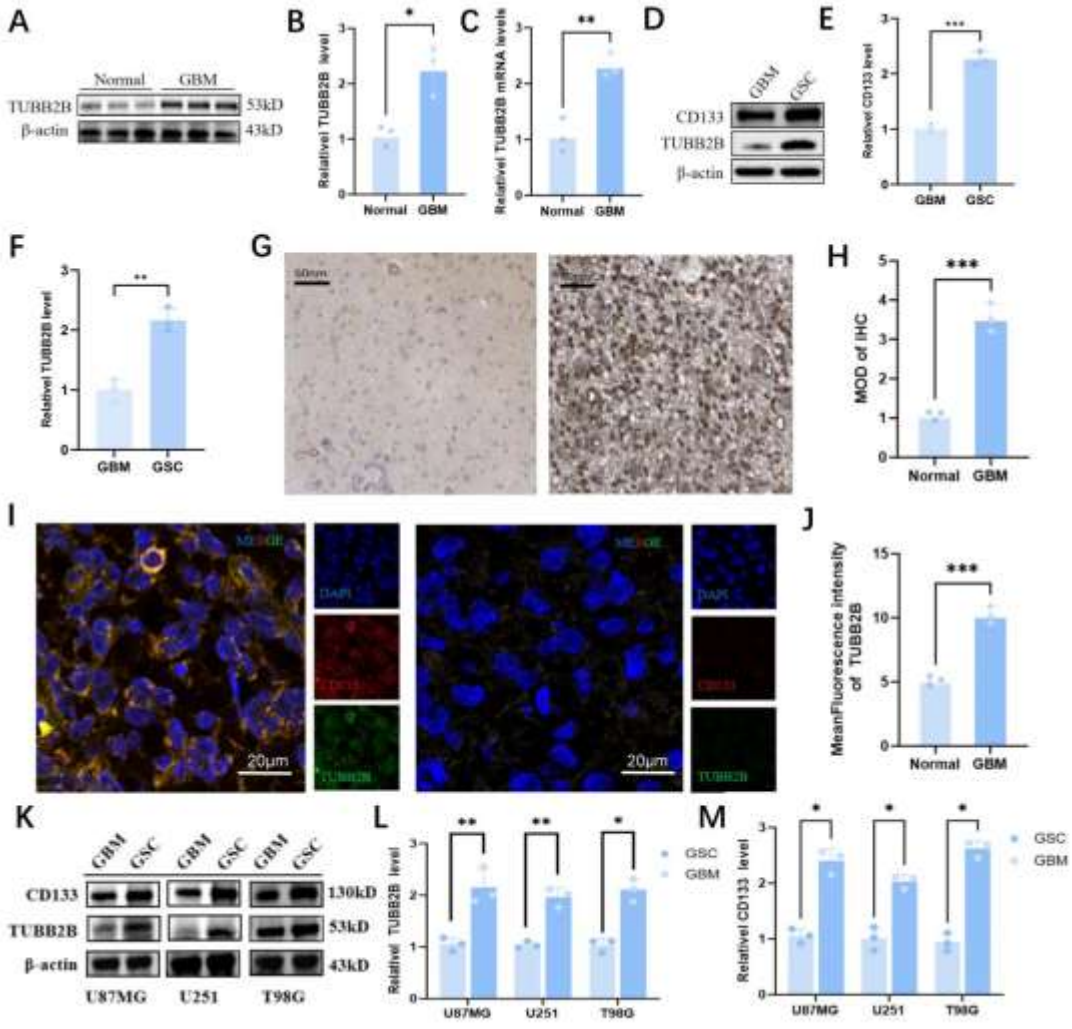


Figure 9. Expression and stemness verification of TUBB2B in GBM. (**A-B**) Western blot analysis demonstrated that TUBB2B was significantly upregulated in GBM tissues. (**C**) qRT-PCR showed that the mRNA level of TUBB2B was significantly elevated in GBM tissues. (**D-F**) In GSC derived from GBM, CD133 and TUBB2B show high expression. (**G-H**) IHC validation of TUBB2B expression in GBM. (**I-J**) IF showed that TUBB2B and CD133 were simultaneously significantly upregulated in GBM tissues. (**K-M**) In GSC derived from the GBM cell lines (U87MG, U251 and T98G cell lines), CD133 and TUBB2B show high expression.

2.10 shTUBB2B and temozolomide exert therapeutic effects by modulating stemness

We evaluated the expression of GSC markers CD133 and OLG2 in GSC derived from

GBM (**Figure 10A-C**)and U89MG cells (**Figure 10D-F**) following treatment with shTUBB2B and TMZ. The results indicated that both treatments exhibited therapeutic effects, with the combination therapy demonstrating the greatest efficacy. Then we measured the viability of the two types of cells using the CCK-8 assay (**Figure 10G-J**). In parallel, Transwell assays (**Figure 10K-L**) and EdU assays (**Figure 10M-N**) corroborated these findings, showing consistent outcomes.

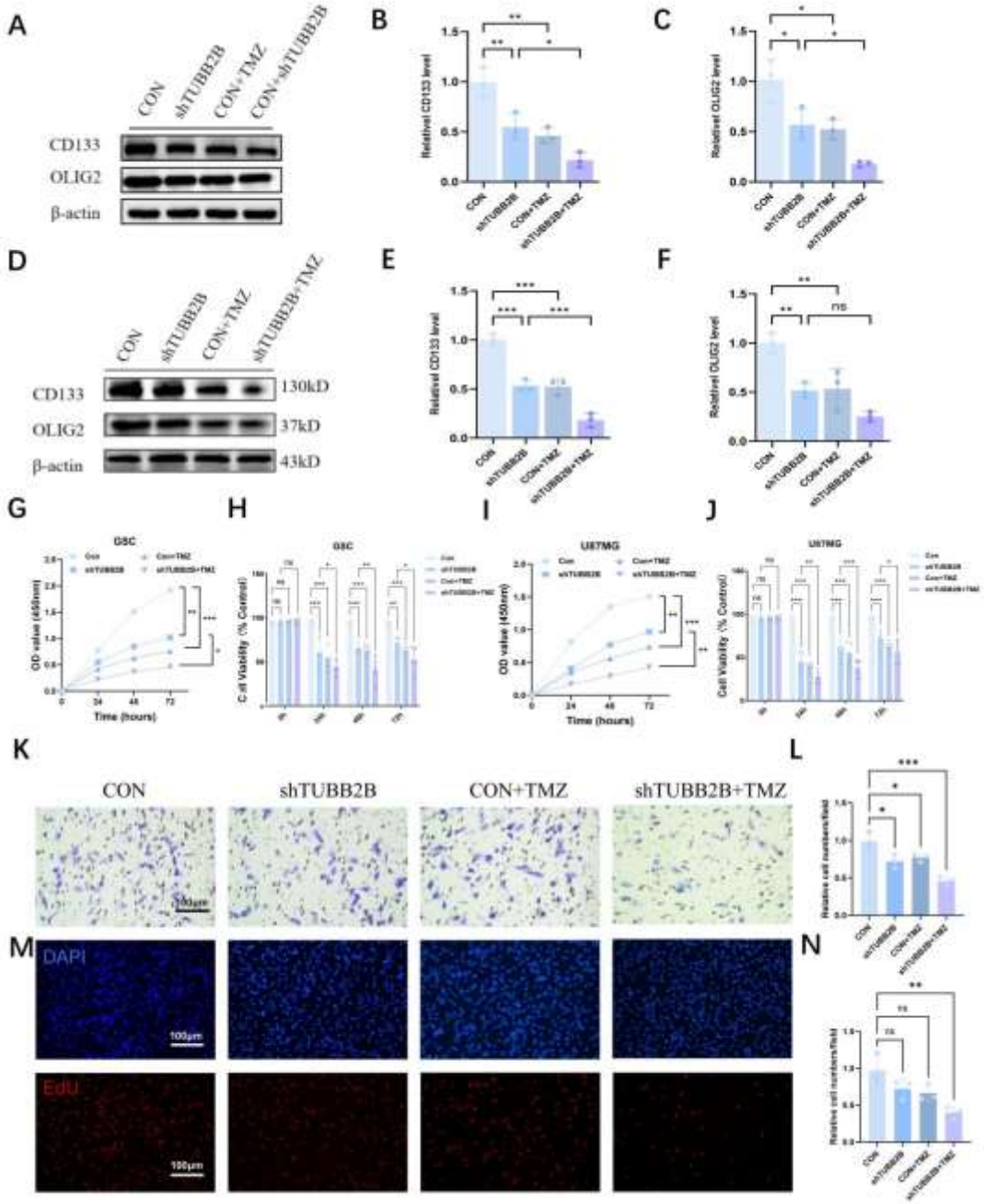


Figure 10. Verification of the therapeutic effects of shTUBB2B and temozolomide. (**A-C**) The expression changes of CD133 and OLIG2 in GSC derived from GBM

treated with shTUBB2B and TMZ. (**D-F**) The expression changes of CD133 and OLIG2 in U87MG treated with shTUBB2B and TMZ. (**G-H**) CCK8 assay of GSC cells derived from GBM. (**I-J**) CCK-8 assay of GSC cells derived from U87MG. (**K-L**) Transwell assays. (**M-N**) EdU assays.

3. Discussion

Glioblastoma stem cells are widely recognized as a critical cell population driving GBM initiation, drug resistance, and recurrence[25-27]. Functionally, these cells possess self-renewal and multipotent differentiation capabilities, and can regenerate tumors in xenograft models, exhibiting biological characteristics similar to normal neural stem cells[28,29]. Furthermore, glioblastoma stem cells play a pivotal role in promoting tumor heterogeneity, immune evasion, and therapeutic tolerance, contributing to the poor prognosis of GBM patients[29,30]. At the molecular biomarker level, glioblastoma stem cells frequently exhibit high expression of stem cell-associated molecules such as CD133. This marker is widely used for the isolation and identification of such cells[31], and $CD133^+$ cells have been demonstrated to possess strong tumor-initiating capacity[32]. However, it is important to note that the concept of glioblastoma stem cells carries multiple biological layers of meaning. At the cellular level, it refers to a subpopulation of cells validated in functional experiments to possess tumor-initiating capacity. At the transcriptomic level, tumor stemness often manifests as a continuum of states associated with differentiation potential, plasticity, and transcriptional complexity. Therefore, relying solely on traditional bulk RNA sequencing or histopathological methods makes it challenging to systematically reveal the dynamic spatial and microenvironmental distribution characteristics of stemness states. Although previous studies have emphasized the central role of glioblastoma stem cells in GBM treatment resistance, most work has focused on single markers or specific signaling pathways[33], lacking a unified framework that integrates transcriptional states, spatial structures, and microenvironmental interactions.

Importantly, our findings should be interpreted in the context of prior single-cell transcriptomic studies that have systematically characterized malignant cell states in glioblastoma. Pioneering work by Couturier et al.[34] demonstrated that GBM tumor cells recapitulate distinct developmental programs, including OPC-like, NPC-like, AC-like, and MES-like states, and that these states can coexist within individual tumors. Similarly, Bhaduri et al.[35] revealed that malignant cells resemble aberrant neurodevelopmental hierarchies, highlighting radial glia‐like and progenitor-like transcriptional programs. Guilhamon et al.[36] further showed that stem-like and progenitor-like populations exhibit region-specific epigenetic and transcriptional regulation, while Richards et al.[37] emphasized the plasticity and dynamic interconversion between these malignant cell states.

Our transcriptionally defined GSC population partially overlaps with previously described OPC-like and NPC-like malignant programs, particularly in terms of high transcriptional complexity, progenitor-associated gene expression, and enrichment in developmental signaling pathways such as EGFR and MAPK. However, rather than assigning stemness to a predefined transcriptional subtype, we employed a quantitative, differentiation-potential‐based framework using CytoTRACE to model stemness as a continuous variable. Against this backdrop, our study integrated large-scale, multi-platform single-cell and spatial transcriptomic data to construct a continuum model of malignant cell differentiation potential in GBM, based on over 338,000 cells from 16 independent studies. Based on CytoTRACE scores and single-cell pseudo-time analysis, we observed that tumor cells do not simply fall into “stem-like” or “non-stem-like” categories. Instead, they transition gradually along a dynamic continuum from stemness-like states with high transcriptional complexity toward relatively differentiated states, forming a dynamic trajectory from CytoTRACE-high populations to DTSC and then to LSC. This aligns with the conventional view that GBM's extreme heterogeneity originates from subpopulations of glioblastoma stem cells [38,39]. It must be emphasized that although the CytoTRACE-overexpressing population showed consistent enrichment with established stem cell-related markers (including PROM1/CD133 and EMT-related

markers), supporting its characterization as a stem cell-associated malignant cell population, more precisely, the GSC defined in this study is a more accurate description of a group of malignant cells rich in stemness characteristics at the transcriptional level, rather than an absolute definition of functional tumor-initiating cells. We found that malignant cells exhibiting this transcriptional state demonstrate more pronounced characteristics in invasiveness, metabolic activity, and signaling pathway activation. Concurrently, DTSC serves as an intermediate bridge in cellular differentiation and tumor evolution. This continuum model offers a novel perspective on GBM recurrence and therapeutic resistance: transcriptionally active stemness-associated states and their transitional subpopulations, with their high phenotypic plasticity and microenvironmental adaptability, may constitute a core driver sustaining tumor heterogeneity. Furthermore, we observe that this GSC population exhibits a spatial tendency to enrich in OPC-like regions and displays activation in signaling pathways such as MAPK and EGFR, suggesting an intrinsic correlation between spatial structure and functional state.

A significant highlight of our study is the integration of digital pathology with molecular omics data to assess the pathological features of GBM. By employing H&E staining and multi-scale feature extraction through deep learning models such as ResNet-50 and CellProfiler, we achieved exceptional precision in quantifying tissue morphology and structural characteristics. Pathological features derived from WSIs revealed distinct patterns associated with GSC, particularly in terms of cell density, granularity, and intensity. By integrating these features into a machine learning model, we developed a robust prognostic tool that stratifies patients into high-risk and low-risk groups based on stemness-related characteristics. The predictive accuracy of this model was rigorously validated through survival curves and ROC analysis, confirming its potential as a clinical tool for personalized treatment strategies. Subsequently, we performed paired analysis of tumor cell spatial colocalization with immune and stromal components, revealing that GSC modulate the immune microenvironment through multiple signaling pathways to achieve self-protection and promote invasion. Notably, we identified significant interaction networks between the

GSC subpopulations and immune-suppressive macrophages and astrocytes, suggesting that tumor stem cells may exploit these non-tumor cells to establish an immune evasion barrier. On one hand, GSC express a variety of immune checkpoint molecules such as PD-L1 and IDO; on the other hand, these subpopulations are spatially enriched in immune "cold" regions, supporting the molecular mechanisms behind the low response rates to tumor immunotherapy. Additionally, the spatial transcriptomic analysis of GSC distribution within tumor tissues highlights the heterogeneity of the TME. We observed that GSC localized to specific regions of the tumor, indicating the presence of niche-like microenvironments that may be critical for maintaining stemness and promoting tumor growth. The ability to map these spatial patterns provides new insights, as it enables the identification of key tumor regions that may require targeted therapeutic interventions.

Among the hub genes identified through machine learning, TUBB2B was found to serve as a critical regulator of GBM stemness. TUBB2B is a subtype of β-tubulin that is predominantly expressed in the brain during embryonic development and plays a crucial role in axon guidance[40]. Loss-of-function mutations in TUBB2B have been associated with congenital neurological disorders[41]. In the context of cancer, recent studies have shown that TUBB2B is overexpressed in hepatocellular carcinoma[42], lung cancer[43], neuroblastoma[44], and prostate cancer[45]. Moreover, elevated expression of TUBB2B has been observed in brain metastases of patients with triple-negative breast cancer[46]. Li et al. demonstrated in vitro that knockdown of TUBB2B inhibited the migration and invasion of GBM cells, whereas its overexpression promoted these processes[47]. However, research on the role of TUBB2B in GSC remains limited. Our experiments further confirmed that TUBB2B is a promising therapeutic target for GBM. Silencing TUBB2B in GBM cell lines enriched with GSC markedly inhibited cell proliferation and tumorigenic capacity. Furthermore, the combined treatment of TMZ and TUBB2B knockdown demonstrated enhanced therapeutic efficacy. These results suggest that TUBB2B could serve as a potential biomarker for targeted therapy and provide novel insights into the development of precision medicine strategies aimed at disrupting

GSC-mediated tumor maintenance.

Although this study integrated single-cell, spatial transcriptomics, and digital pathology data to systematically characterize stemness-related programs in GBM, several limitations remain. First, despite combining multiple independent datasets, residual batch effects cannot be entirely eliminated. Future validation across larger, more diverse human cohorts is needed to enhance the generalizability of these findings. Second, the identification of stemness-associated populations relies on CytoTRACE's modeling of transcriptional complexity. This approach favors capturing transcriptionally active stemness-associated programs and may not fully represent quiescent stem-like subpopulations. Furthermore, proliferative or metabolically active states may exhibit some overlap with transcriptional complexity signals. In spatial transcriptomics, so-called GSC activity reflects the projection of stemness-related gene sets rather than a direct determination of discrete GSC cell identity. Its spatial colocalization with OPC-like regions more likely indicates partial consistency at the transcriptional program level rather than complete overlap of cell populations. Future studies could systematically compare different malignant programs (e.g., OPC-like signatures) within the same integrated spatio-pathological-prognostic framework. Fourth, the prognostic model is constructed based on morphological features extracted from whole-slide images, with stemness-related genes used solely for molecular interpretation through correlation alignment. Thus, the association between morphological risk and stemness programs remains interpretive and does not establish causality. Fifth, candidate drug screening via CMap represents hypothesis generation and does not constitute direct GBM-specific drug sensitivity evidence; further validation in relevant models and pharmacogenomic databases is required. Finally, although TUBB2B has undergone preliminary functional validation, its mechanism and translational potential require deeper investigation.

4. Methods

4.1 Data collection and processing

The scRNA-seq data analyzed in this study were derived from the previously

compiled and coordinated glioblastoma single-cell atlas by Ruiz-Moreno et al[48]. Bulk RNA-seq data and pathological imaging data were obtained from the TCGA database (https://portal.gdc.cancer.gov/). Rigorous quality control procedures were implemented. This study includes a stRNA-seq sample of GBM, and the sample is identified by the accession number GSM5833536 (**Supplementary Table 10**).

The criteria for cell inclusion were as follows: a minimum of 500 detected genes, at least 1,000 unique molecular identifier (UMI) counts, and a mitochondrial gene expression proportion below 30%, in order to exclude low-quality or potentially damaged cells. Principal component analysis (PCA) was conducted on the normalized expression matrix following data integration. The top 20 principal components were extracted using the "RunPCA" function to capture the primary sources of variation within the dataset. These components were subsequently utilized as input for the "FindNeighbors" function to construct a k-nearest neighbor graph representing the relationships among cells. Clustering analysis was performed using the "FindClusters" function, with the resolution parameter adjusted according to the complexity of the underlying cell types. A resolution value of 0.6 was consistently applied across all samples to ensure both granularity and stability in cluster identification. To visualize the data in a two-dimensional space, the "RunUMAP" method was employed using the same set of principal components and default optimization settings as previously defined. This approach enabled effective dimensionality reduction and visualization through nonlinear manifold learning, thereby revealing the intrinsic cellular population structure and potential transitions. Furthermore, the "FindAllMarkers" function was applied with a minimum percentage threshold (min.pct) of 0.25 to identify cluster-specific marker genes, ensuring that selected genes were significantly expressed in at least 25% of the target cluster cells.

4.2 Targeting the glioblastoma stem cells of GBM

Following this, the CytoTRACE algorithm was applied to evaluate the differentiation status of tumor cells. This algorithm has been extensively validated across large-scale datasets and has shown robust performance. CytoTRACE computes a gene expression

matrix to assign a stemness score to each individual cell, with scores ranging from 0 to 1. Higher scores indicate greater stemness, or correspondingly lower levels of differentiation. To classify the cells, we categorized them based on quartiles of the CytoTRACE scores: low stem cells (LSC, ⩽ 25th percentile), dynamic transition stem cells (DTSC, 25th to 75th percentile), and glioblastoma stem cells (GSC, ⩾ 75th percentile). This quartile-based classification strategy is data-driven and non-arbitrary, enabling an objective characterization of CNV heterogeneity among tumor cells. It facilitates the identification of GSC, which is essential for investigating CNV progression trajectories and their relationships with differentiation potential and the immune microenvironment.

4.3 Observed/expected (Ro/e) enrichment analysis

To evaluate the enrichment of GSC, DTSC and LSC across different tumor cell subpopulations, an Ro/e enrichment analysis was performed. For each stemness group, the expected proportion was calculated as the global fraction of that group among all tumor cells. The observed proportion was defined as the fraction of the same stemness group within a specific annotated cell subpopulation. The Ro/e ratio was calculated as the observed proportion divided by the expected proportion, where Ro/e > 1 indicates enrichment and Ro/e < 1 indicates depletion. Statistical significance of enrichment or depletion was assessed using Fisher’s exact test by comparing the number of cells belonging to a given stemness group within each cell subpopulation against all remaining tumor cells. P values were adjusted for multiple comparisons using the false discovery rate (FDR) method. All analyses were conducted using R software (version 4.1.3).

4.4 Cell communication and pseudotime analysis

We utilized the "Monocle3[49]" R package to construct pseudo-temporal trajectories, allowing for the mapping of differentiation processes and cellular transitions in GBM. To further investigate intercellular communication within the TME, we employed the "CellChat[50]" R package. Using the netVisual_bubble function, we generated bubble plots to visualize key ligand-receptor interactions, which facilitated the identification

of critical signaling networks potentially involved in tumor progression, immune evasion, and therapeutic resistance.

4.5 The pipeline of high-dimensional WGCNA (hdWGCNA)

To identify the key genes that maintain GSC, rather than isolated differentially expressed genes, we applied high-dimensional hdWGCNA to the scRNA-seq data. Although differential expression analysis highlights individual genes related to the stem cell state, it fails to capture the higher-order transcriptional organization or coordinated regulatory modules that may drive the GSC identity. hdWGCNA is specifically designed for single-cell data and can identify biologically significant co-expression modules, while also reducing the noise caused by the reduction technique in the middle cells. The hdWGCNA package (version 0.2.2) was utilized to perform weighted gene co-expression network analysis on single-cell data[51]. Initially, genes that were expressed in at least 5% of the cells were selected as input. Subsequently, the "MetacellsByGroups" function was applied to generate a metacell-based gene expression matrix. The "TestSoftPowers" function was then used to determine the optimal soft-thresholding power. Finally, the "ConstructNetwork" function was employed to build the co-expression network.

4.6 Multi-scale feature analysis based on ResNet-50 and CellProfiler

To extract key pathological features from whole-slide images (WSIs) of GBM patients for more accurate diagnostic and prognostic evaluation, we propose a multi-dimensional feature learning approach that integrates histopathological image analysis with the ResNet-50 deep learning model. First, we retrieved hematoxylin- and eosin-stained WSIs of GBM from the TCGA database at a magnification level of 20×. Given the large size of WSIs, they cannot be directly processed by deep neural networks[52]. Therefore, each WSI was partitioned into non-overlapping image patches of 512×512 pixels. Subsequently, the Sobel edge detection algorithm was employed to identify patches containing tissue structures. The Otsu thresholding method was further applied for background segmentation, and only those patches with

tissue content exceeding 80% were retained for downstream analysis. To mitigate the effects of staining variation across different samples, all selected image patches underwent color normalization using the Macenko algorithm. The tile size was adjusted to 224×224 pixels to conform to the input specifications of the ResNet-50 model. The pre-trained ResNet-50 model was implemented using the PyTorch framework, and the final fully connected layer was removed in order to extract deep features from the image tiles. Each tile was subsequently transformed into a 2,048-dimensional feature vector via global average pooling. Given that the ResNet-50 model was originally trained on natural images and may contain features irrelevant to histopathological data, an autoencoder module was introduced to reduce the dimensionality of the feature vectors from 2,048 to 512 dimensions. This autoencoder comprises an encoder and a decoder. The encoder consists of a fully connected layer followed by a ReLU activation function, which maps the input into a 512-dimensional latent space, while the decoder reconstructs the input from this compressed representation. This dimensionality reduction process effectively eliminates redundant information, reduces computational complexity, and enhances the model's generalization capability. Following feature extraction and compression, a multi-layer perceptron (MLP) classifier was developed, where the input corresponds to the compressed 512-dimensional feature vectors and the output represents the molecular subtypes and prognostic outcomes of GBM. The model was trained on the training dataset and evaluated on independent validation and test datasets. Its performance was assessed using metrics such as accuracy, sensitivity, specificity, and AUC, which were calculated through cross-validation and confusion matrix analysis.

Pathological features were extracted from each H&E-stained image using CellProfiler (version 4.2.5)[53]. The "ColorToGray" module was employed to convert H&E-stained images into grayscale images. Subsequently, the "UnmixColors" module was applied to separate the H&E-stained images into hematoxylin-only and eosin-only grayscale images. The "ColorToGray" module was again utilized, based on the "Combine" method, to generate grayscale images for subsequent analysis. Image

quality metrics—including blur, intensity, and threshold features—were assessed using the "MeasureImageQuality" and "MeasureImageIntensity" modules for the grayscale H&E, hematoxylin, and eosin images. The Otsu algorithm was applied to automatically determine the threshold for each image, enabling the segmentation of foreground and background regions. The "MeasureColocalization" module was used to compute the pixel-wise correlation between colocalization and intensity features across the entire image. Finally, the "MeasureGranularity" module was employed to evaluate the granularity characteristics of each image.

4.7 Machine learning benchmark models predict the prognosis of GBM

To rigorously evaluate the prognostic value of ResNet-50 and CellProfiler-derived features in GBM survival prediction, we implemented an integrative computational framework combining deep learning feature extraction with advanced single-cell transcriptomic analytics. Initial feature screening was performed through univariate Cox proportional hazards modeling, where each convolutional neural network-derived morphological feature was systematically interrogated for association with OS using a FDR-corrected significance threshold of $q<0.05$. To ensure feature selection robustness against sampling bias, we employed an ensemble bootstrap aggregation approach with 10,000 iterations, retaining only features demonstrating consistent selection frequencies exceeding the 95th percentile of the null distribution. For predictive modeling, we conducted comprehensive benchmarking of seven state-of-the-art machine learning architectures implemented through the mlr3 ecosystem in R, including: 1) kernel-based k-nearest neighbors (KKNN) with adaptive bandwidth selection, 2) regularized linear discriminant analysis (LDA) with elastic net penalty, 3) Bayesian naive classifiers with kernel density estimation (NB), 4) ℓ2-penalized logistic regression with trust region optimization, 5) permutation-corrected random forests (Ranger) incorporating out-of-bag impurity measures, 6) survival-optimized recursive partitioning (RPART) with complexity parameter tuning, and 7) extreme gradient boosting (XGBoost) with early stopping

rounds. The cohort was partitioned under stratified random sampling (80:20) preserving the event rate distribution, with model optimization performed through nested cross-validation - employing an inner folds for hyperparameter tuning via Bayesian optimization and 10 outer folds for unbiased performance estimation. To enhance biological interpretability, we computed patient-specific risk scores through non-negative matrix factorization of selected features, establishing prognostic stratification thresholds via maximally selected rank statistics. Survival disparities between risk groups were quantified through weighted Kaplan-Meier estimation with log-rank testing adjusted for multiple comparisons. Predictive accuracy was rigorously assessed through time-dependent receiver operating characteristic (ROC) analysis at clinically relevant endpoints (1/3/5-year OS), with area under the curve (AUC) confidence intervals derived from 1000 bootstrap replicates.

4.8 Evaluation of immunotherapy and drug sensitivity

To conduct an unsupervised comparative analysis of the transcriptional profiles across heterogeneous patient cohorts exhibiting differential responses to immunotherapy, this study employed the SubMap algorithm to systematically evaluate the similarity of gene expression patterns among various patient samples. This approach was utilized to identify potential consistencies in clinical response patterns. Furthermore, the Tumor Immune Dysfunction and Exclusion (TIDE)[54] scoring framework was applied to estimate the activity of tumor immune escape mechanisms based on gene expression data derived from tumor tissues. TIDE integrates multiple layers of immune suppression-related signals and models the potential for tumor cells to develop resistance to treatment through immune evasion within the tumor microenvironment. For the assessment of drug sensitivity, data were obtained from two publicly available databases: the Cancer Therapeutics Response Portal (CTRP) and Profiling Relative Inhibition Simulation in Mixtures (PRISM). The AUC was used as a quantitative metric to evaluate the sensitivity of cell lines to various pharmacological agents, with higher AUC values indicating reduced drug inhibitory efficacy and correspondingly lower sensitivity.

4.9 Patients and samples

GBM tissue samples and adjacent normal brain tissue specimens were collected from patients diagnosed with GBM who underwent surgical resection at the Affiliated Hospital of Qingdao University. And it was approved by the Ethics Committee of Qingdao University Affiliated Hospital (QYFY WZLL 30507). Written informed consent was obtained from each participant in accordance with the Declaration of Helsinki. Prior to sample collection and diagnosed by two pathologists under blinded conditions to ensure diagnostic accuracy and objectivity.

4.10 Cell culture

According to the established protocol, GBM cells and GSC were isolated from primary surgical GBM biopsy specimens obtained from the Affiliated Hospital of Qingdao University. All participants were fully informed about the study, and written informed consent was obtained prior to sample collection. To reduce the artifacts in in vitro cell culture, patient-derived xenografts are used as a renewable source for the proliferation of GSCs. GSC was cultured in the neural basal medium (Invitrogen) in the form of neurosphere. It was supplemented with 2% B27 supplement (Life Technologies), 1% L-glutamine, 1% sodium pyruvate, 20 ng/mL bFGF and EGF (R&D Systems). All experiments were conducted with the cells in the spherical form for preservation and culture. For immunofluorescence analysis, the cells were cultured in a monolayer for easy imaging. In GBM cell lines (U87MG, U251 and T98G), GSC-like populations were operationally defined as CD133-positive cells isolated by magnetic-activated cell sorting (MACS). After sorting, cells were further cultured under serum-free stem cell conditions (DMEM/F12 supplemented with B27, EGF, and bFGF) to promote tumorsphere formation and maintain stem-like properties. The enrichment of GSC characteristics was validated by the expression of stem cell markers (CD133, OLIG2) using WB and IF assays. Plasmid transfections were carried out using Lipofectamine 3000 according to the manufacturer's guidelines. For gene knockdown experiments, the following short hairpin RNA (shRNA) sequences were used: shTUBB2B-F:

CCGGGATGACATCAATGTAACATTTCTCGAGAAATGTT
ACATTGATGTCATCTTTTT, shTUBB2B-R: AATTAAAAAGATGACATCAA
TGTAACATTTCTCGAGAAATGTTACATTGATGTCATC.

4.11 Immunofluorescence (IF)

Cell and tumor tissue sections were processed for immunofluorescence staining and examined using a confocal microscope. For cell samples, membrane proteins were labeled by incubation with primary antibodies at 4 °C for 12 hours, followed by treatment with secondary antibodies. Intracellular proteins were fixed and permeabilized using phosphate-buffered saline (PBS) containing 0.1% Triton X-100. Nuclei were stained with DAPI. Tissue samples were subjected to paraffin embedding and sectioning, and subsequently immunostained with the specified antibodies.

4.12 Immunohistochemistry (IHC)

IHC was conducted on paraffin-embedded tissue sections to assess the expression level of TUBB2B in GBM and normal brain tissues. The tissue sections were dewaxed and rehydrated through a graded ethanol series, followed by overnight incubation with the primary antibody at 4°C. Following thorough washing with phosphate-buffered saline (PBS), the sections were exposed to the corresponding secondary antibody and visualized using 3,3'-diaminobenzidine (DAB) as the chromogenic substrate. Subsequently, the sections were counterstained with hematoxylin and examined under an optical microscope.

4.13 Western Blotting (WB)

Cells or GBM tissue samples were lysed using RIPA buffer on ice for 30 minutes. After lysis, the samples were centrifuged at 4°C to remove any cellular debris, and the supernatants were collected. To denature the proteins, the lysates were heated at 100°C for 5 minutes in SDS sample buffer. Proteins were then separated by SDS-PAGE and transferred to PVDF membranes. Blocking was performed using a solution of 5% skim milk at room temperature for 2 hours, after which the membranes were probed with primary and secondary antibodies specific to the targets of interest.

4.14 Quantitative Real-Time PCR (qRT-PCR)

Total RNA was isolated from both tissue specimens and cultured cells using TRIzol reagent (Beyotime Biotechnology). Following RNA extraction, complementary DNA (cDNA) was synthesized, and qRT-PCR was carried out with PowerUp™ SYBR™ Green Master Mix (Thermo Fisher Scientific) on an ABI Prism 7500 Real-Time PCR System. The primer sequences used in this analysis are provided in **Supplementary Table 11**.

4.15 EdU proliferation assay

Cell proliferation was assessed using an EdU incorporation kit (C0071S; Beyotime, China) in accordance with the manufacturer's instructions. GSC were seeded in 6-well plates and cultured until reaching approximately 70% confluence. Following this, EdU solution was added to a final concentration of 10 μM, and the cells were incubated for 2 hours. After incubation, cells were fixed using the provided cell fixation solution, and EdU staining was carried out following the kit's protocol. Finally, the number of EdU-positive cells was determined by fluorescence microscopy to evaluate the proliferative capacity of the cells.

4.16 Transwell assay

Cell migration and invasion assays were conducted using Transwell chambers. For the migration assay, GSC were seeded in the upper chamber, while culture medium was added to the lower chamber, followed by incubation for 24 hours. In the invasion assay, the upper chamber was pre-coated with Matrigel (8.0-μm pore size; BD Bioscience) and incubated for 2 hours. Following gel solidification, cells were seeded and incubated for an additional 24 hours. Non-migrated or non-invaded cells remaining in the upper chamber were carefully removed with a cotton swab. The migrated or invaded cells were then fixed with methanol, stained with crystal violet, and counted under a microscope to assess cell migration and invasion capacity.

4.17 Statistical analysis

All statistical analyses were conducted using R software (version 4.1.3). For

comparing continuous variables between two groups, either the Wilcoxon test or the t-test was applied, depending on the data distribution. Categorical variables were analyzed using the χ^2 test or Fisher's exact test, as appropriate. Spearman's rank correlation coefficient was employed to assess the relationship between two continuous variables. OS was evaluated using Kaplan-Meier survival analysis, and differences between groups were tested using the log-rank test. All p-values were derived from two-sided tests and adjusted for multiple comparisons using the FDR method. A statistically significant result was defined as $p < 0.05$.

Data Availability

The datasets presented in this study can be found in online repositories (https://www.cancer.gov/ccg/research/genome-sequencing/tcga, https://www.ncbi.nlm.nih.gov/geo/). The names of the repository/repositories and accession number(s) can be found in the article/ Supplementary Material. The custom code and scripts used during the current study are available from the corresponding author upon reasonable request.

Acknowledgments

The large-scale integration of scRNA-seq data from multiple studies benefited greatly from the recently released GBmap resource by Ruiz-Moreno et al. This resource provided a solid and coordinated foundation for our analyses of stemness, spatial distribution, and prognosis. The authors declare that no financial support was received for the research, authorship, and publication of this article.

Author Contributions

YFX: Writing – review & editing, Writing – original draft, Formal analysis, Data curation, Conceptualization. JPW and JSW: Formal analysis, Data curation, Writing – review & editing. ZXG: Conceptualization, Writing – review & editing. HTL: Validation, Formal analysis, Writing – review & editing. SFL: Resources, Writing – review & editing, Software. YGF and SHH: Validation, Supervision, Writing – review & editing. PG: Methodology, Funding acquisition, Writing – review & editing.

Competing Interests

The authors declare no competing financial or non-financial interests.

Funding Statement

The author(s) declare that no financial support was received for the research.

Ethics approval and consent to participate' statement for patients

This study (Mapping the Stemness Features of Glioblastoma to Reveal Its Heterogeneity and Drug Resistance) has been approved by the Ethics Committee of Qingdao University Affiliated Hospital (QYFY WZLL 30507), with approval date: August 19, 2025. All participants have provided written informed consent in accordance with the requirements of the Declaration of Helsinki.

AI use transparently

The authors declare that they have not used AI-generated work in this manuscript

Reference

1. Schaff, L. R. & Mellinghoff, I. K. Glioblastoma and Other Primary Brain Malignancies in Adults: A Review. *Jama* **329**, 574-587 (2023).
2. Shergalis, A., Bankhead, A., 3rd, Luesakul, U., Muangsin, N. & Neamati, N. Current Challenges and Opportunities in Treating Glioblastoma. *Pharmacol Rev* **70**, 412-445 (2018).
3. Bikfalvi, A. *et al.* Challenges in glioblastoma research: focus on the tumor microenvironment. *Trends Cancer* **9**, 9-27 (2023).
4. Pouyan, A. *et al.* Glioblastoma multiforme: insights into pathogenesis, key signaling pathways, and therapeutic strategies. *Mol Cancer* **24**, 58 (2025).
5. Khan, F. *et al.* Macrophages and microglia in glioblastoma: heterogeneity, plasticity, and therapy. *J Clin Invest* **133** (2023).
6. Wu, W. *et al.* Glioblastoma multiforme (GBM): An overview of current therapies and mechanisms of resistance. *Pharmacol Res* **171**, 105780 (2021).
7. Cloughesy, T. F., Cavenee, W. K. & Mischel, P. S. Glioblastoma: from molecular pathology to targeted treatment. *Annu Rev Pathol* **9**, 1-25 (2014).
8. Hawly, J., Murcar, M. G., Schcolnik-Cabrera, A. & Issa, M. E. Glioblastoma stem cell metabolism and immunity. *Cancer Metastasis Rev* **43**, 1015-1035 (2024).

9. LeBlanc, V. G. *et al.* Single-cell landscapes of primary glioblastomas and matched explants and cell lines show variable retention of inter- and intratumor heterogeneity. *Cancer Cell* **40**, 379-392.e379 (2022).
10. Kang, Y. J. *et al.* Contribution of classical end-joining to PTEN inactivation in p53-mediated glioblastoma formation and drug-resistant survival. *Nat Commun* **8**, 14013 (2017).
11. Djuzenova, C. S. *et al.* Actin cytoskeleton organization, cell surface modification and invasion rate of 5 glioblastoma cell lines differing in PTEN and p53 status. *Exp Cell Res* **330**, 346-357 (2015).
12. Wang, Z., Zhang, H., Xu, S., Liu, Z. & Cheng, Q. The adaptive transition of glioblastoma stem cells and its implications on treatments. *Signal Transduct Target Ther* **6**, 124 (2021).
13. Huang, Z., Cheng, L., Guryanova, O. A., Wu, Q. & Bao, S. Cancer stem cells in glioblastoma--molecular signaling and therapeutic targeting. *Protein Cell* **1**, 638-655 (2010).
14. Biserova, K., Jakovlevs, A., Uljanovs, R. & Strumfa, I. Cancer Stem Cells: Significance in Origin, Pathogenesis and Treatment of Glioblastoma. *Cells* **10** (2021).
15. Bradley, C. A. Glioblastoma: Stem cells - masters of their fates. *Nat Rev Cancer* **17**, 574-575 (2017).
16. Beier, D., Schulz, J. B. & Beier, C. P. Chemoresistance of glioblastoma cancer stem cells--much more complex than expected. *Mol Cancer* **10**, 128 (2011).
17. Xu, Y. *et al.* Integrated analysis of single-cell RNA-seq and spatial transcriptomics to identify the lactylation-related protein TUBB2A as a potential biomarker for glioblastoma in cancer cells by machine learning. *Front Immunol* **16**, 1601533 (2025).
18. Wang, Z. *et al.* Single-cell RNA sequencing deconvolutes the in vivo heterogeneity of human bone marrow-derived mesenchymal stem cells. *Int J Biol Sci* **17**, 4192-4206 (2021).

19. Tani, S. *et al.* Stem cell-based modeling and single-cell multiomics reveal gene-regulatory mechanisms underlying human skeletal development. *Cell Rep* **42**, 112276 (2023).
20. Liu, Y. *et al.* Single-cell and spatial transcriptome analyses reveal tertiary lymphoid structures linked to tumour progression and immunotherapy response in nasopharyngeal carcinoma. *Nat Commun* **15**, 7713 (2024).
21. El Nahhas, O. S. M. *et al.* From whole-slide image to biomarker prediction: end-to-end weakly supervised deep learning in computational pathology. *Nat Protoc* **20**, 293-316 (2025).
22. Rashidi, H. H. *et al.* Generative Artificial Intelligence in Pathology and Medicine: A Deeper Dive. *Mod Pathol* **38**, 100687 (2025).
23. Li, Z. *et al.* Integrating computational pathology and multi-transcriptomics to characterize lung adenocarcinoma heterogeneity and prognostic modeling. *Int J Surg* (2025).
24. Feng, B. *et al.* Ligand-receptor interactions combined with histopathology for improved prognostic modeling in HPV-negative head and neck squamous cell carcinoma. *NPJ Precis Oncol* **9**, 57 (2025).
25. Cheng, L. *et al.* Glioblastoma stem cells generate vascular pericytes to support vessel function and tumor growth. *Cell* **153**, 139-152 (2013).
26. Chen, J. *et al.* A restricted cell population propagates glioblastoma growth after chemotherapy. *Nature* **488**, 522-526 (2012).
27. Bao, S. *et al.* Glioma stem cells promote radioresistance by preferential activation of the DNA damage response. *Nature* **444**, 756-760 (2006).
28. Xie, X. P. *et al.* Glioblastoma functional heterogeneity and enrichment of cancer stem cells with tumor recurrence. *Neuron* **112**, 4017-4032.e4016 (2024).
29. Tang, J., Amin, M. A. & Campian, J. L. Glioblastoma Stem Cells at the Nexus of Tumor Heterogeneity, Immune Evasion, and Therapeutic Resistance. *Cells* **14** (2025).

30. Ghosh, N., Chatterjee, D. & Datta, A. Tumor heterogeneity and resistance in glioblastoma: the role of stem cells. *Apoptosis* **30**, 1695-1729 (2025).
31. Joyce, T., Jagasia, S., Tasci, E., Camphausen, K. & Krauze, A. V. An Overview of CD133 as a Functional Unit of Prognosis and Treatment Resistance in Glioblastoma. *Curr Oncol* **30**, 8278-8293 (2023).
32. Zeppernick, F. *et al.* Stem cell marker CD133 affects clinical outcome in glioma patients. *Clin Cancer Res* **14**, 123-129 (2008).
33. Liu, X. *et al.* Transformed astrocytes confer temozolomide resistance on glioblastoma via delivering ALKBH7 to enhance APNG expression after educating by glioblastoma stem cells-derived exosomes. *CNS Neurosci Ther* **30**, e14599 (2024).
34. Couturier, C. P. *et al.* Single-cell RNA-seq reveals that glioblastoma recapitulates a normal neurodevelopmental hierarchy. *Nat Commun* **11**, 3406 (2020).
35. Bhaduri, A. *et al.* Outer Radial Glia-like Cancer Stem Cells Contribute to Heterogeneity of Glioblastoma. *Cell Stem Cell* **26**, 48-63.e46 (2020).
36. Guilhamon, P. *et al.* Single-cell chromatin accessibility profiling of glioblastoma identifies an invasive cancer stem cell population associated with lower survival. *Elife* **10** (2021).
37. Richards, L. M. *et al.* Gradient of Developmental and Injury Response transcriptional states defines functional vulnerabilities underpinning glioblastoma heterogeneity. *Nat Cancer* **2**, 157-173 (2021).
38. Tabatabai, G. & Weller, M. Glioblastoma stem cells. *Cell Tissue Res* **343**, 459-465 (2011).
39. Persano, L., Rampazzo, E., Basso, G. & Viola, G. Glioblastoma cancer stem cells: role of the microenvironment and therapeutic targeting. *Biochem Pharmacol* **85**, 612-622 (2013).
40. Breuss, M. W., Leca, I., Gstrein, T., Hansen, A. H. & Keays, D. A. Tubulins and brain development - The origins of functional specification. *Mol Cell Neurosci* **84**, 58-67 (2017).

41. Cederquist, G. Y. *et al.* An inherited TUBB2B mutation alters a kinesin-binding site and causes polymicrogyria, CFEOM and axon dysinnervation. *Hum Mol Genet* **21**, 5484-5499 (2012).

42. Wang, X. *et al.* TUBB2B facilitates progression of hepatocellular carcinoma by regulating cholesterol metabolism through targeting HNF4A/CYP27A1. *Cell Death Dis* **14**, 179 (2023).

43. Jiang, W. *et al.* Prognostic Signature for Lung Adenocarcinoma Patients Based on Cell-Cycle-Related Genes. *Front Cell Dev Biol* **9**, 655950 (2021).

44. Liu, J. & Li, Y. Upregulation of MAPK10, TUBB2B and RASL11B may contribute to the development of neuroblastoma. *Mol Med Rep* **20**, 3475-3486 (2019).

45. Liotti, A. *et al.* Periprostatic adipose tissue promotes prostate cancer resistance to docetaxel by paracrine IGF-1 upregulation of TUBB2B beta-tubulin isoform. *Prostate* **81**, 407-417 (2021).

46. He, Q. *et al.* Targeting TUBB2B inhibits triple-negative breast cancer growth and brain-metastatic colonization. *J Exp Clin Cancer Res* **44**, 55 (2025).

47. Li, J. *et al.* TUBB2B regulates epithelial-mesenchymal transition via interaction with Vimentin to promote glioma migration and invasion. *Cancer Cell Int* **24**, 423 (2024).

48. Ruiz-Moreno, C. *et al.* Charting the Single-Cell and Spatial Landscape of IDH-Wildtype Glioblastoma with GBmap. *Neuro Oncol* (2025).

49. Zhao, A. Y. *et al.* Single-Cell Analysis Reveals Novel Immune Perturbations in Fibrotic Hypersensitivity Pneumonitis. *Am J Respir Crit Care Med* **210**, 1252-1266 (2024).

50. Jin, S., Plikus, M. V. & Nie, Q. CellChat for systematic analysis of cell-cell communication from single-cell transcriptomics. *Nat Protoc* **20**, 180-219 (2025).

51. Xu, Y. *et al.* Integrated analysis of single-cell sequencing and machine learning identifies a signature based on monocyte/macrophage hub genes to

analyze the intracranial aneurysm associated immune microenvironment. *Front Immunol* **15**, 1397475 (2024).

52. Hoang, D. T. *et al.* Prediction of DNA methylation-based tumor types from histopathology in central nervous system tumors with deep learning. *Nat Med* **30**, 1952-1961 (2024).

53. Wan, Q. *et al.* Integrating pathomics and deep learning for subtyping uveal melanoma: identifying high-risk immune infiltration profiles. *Front Immunol* **16**, 1585097 (2025).

54. Yang, H. *et al.* Identification of lactylation related model to predict prognostic, tumor infiltrating immunocytes and response of immunotherapy in gastric cancer. *Front Immunol* **14**, 1149989 (2023).

Figure Captions

Figure 1. Flowchart of the process mechanism of this study.

Figure 2. Mapping the single-cell atlas of GBM and identification of GSC subpopulations. **(A)** A single-cell atlas was drawn by integrating 338,564 cells from 16 studies. **(B)** Generate single-cell maps for each sample. **(C)** The UMAP plot shows that 20 cell subpopulations were identified. **(D-G)** UMAP visualization highlights the expression patterns of representative marker genes for each cell type. **(H-I)** Cytotrace evaluates the stemness of cells. Based on the IQR, cells are categorized into three distinct groups: GSC. **(J-K)** The UMAP plot illustrates the spatial distribution patterns of these three cell groups. **(L)** Pseudotime trajectory analysis demonstrates the progressive transition from GSC to the LSC state, emphasizing the gradual alterations in genomic instability throughout the process of cell differentiation. **(M-N)** A Ro/e analysis of the enrichment of three groups of cells in different cell subpopulations.

Figure 3. Inter-cellular communication of GSC and enriched metabolic pathways. **(A)** The intercellular interaction network illustrates the number (left panel) and strength (right panel) of interactions among GSC, DTSC, LSC and other cell types. **(B)** The interaction quantity and weight/strength of cellular interactions within the

communication network of GBM. **(C)** Scatter plots depicting the interaction strength between outgoing and incoming within each cell subpopulation indicate that GSC exhibit the highest outgoing interaction strength. **(D-E)** The ligand-receptor interaction levels between GSC and LSC, as well as those involving other cell types, were quantified. **(F)** Pathway enrichment analysis of GSC, DTSC and LSC. **(G)** Bubble chart depicting selected ligand-receptor pairs enriched in GSC, DTSC, LSC and other cell types. **(H)** Drug sensitivity analysis of GSC. **(I)** The metabolic pathway enrichment analysis of GSC, DTSC and LSC revealed that GSC exhibited significant upregulation across all metabolic pathways.

Figure 4. The hdWGCNA analysis identified the magenta, green, red, blue, and turquoise modules as the five core modules significantly correlated with the GSC group. (**A**) A scale-free network was constructed using a soft thresholding power of 10. (**B**) The 12 gene modules within this network were visualized using a dendrogram. (**C**) Differential expression levels of each gene module were assessed across the GSC, DTSC, and LSC groups. (**D**) The distribution patterns of these 12 gene modules were analyzed specifically within the GSC group. (**E**) Correlation analysis was conducted among the 12 gene modules. (**F**) GSC activity was validated in both GBM tissues and normal brain tissues.

Figure 5. Spatial transcriptome analysis assesses the spatial distribution of cell stemness. (A) H&E staining revealed clearly defined histological regions within the stRNA samples. (B) A spatially resolved metabolic map of GSC. (C) GBM tissue architecture inferred through unsupervised clustering analysis.

Figure 6. A comprehensive prognostic model for glioblastoma integrating pathological and deep learning features. (**A**) Flowchart illustrating the feature extraction process using CellProfiler and the ResNet-50 model. (**B**) Schematic representation of the nested cross-validation framework applied across seven survival analysis algorithms. (**C**) Univariate regression analysis identified six key prognostic features associated with GBM. (**D-E**) Comparative evaluation of model performance using C-index and integrated Brier score (IBS) metrics. (**F-G**) Kaplan-Meier survival curves stratifying patients into high-risk and low-risk groups. (**H-I**) ROC curves

assessing the model's predictive accuracy for 1-year, 2-year, and 3-year overall survival outcomes.

Figure 7. Characterization of the immune microenvironment and identification of potential therapeutic agents in high-risk and low-risk GBM patients. (**A**) Box plots depicting the distribution of immune cell characteristics in high-risk and low-risk groups. (**B**) Representative histological images illustrating variations in immune cell infiltration between high-risk (upper panel) and low-risk (lower panel) patients. (**C**) Pathway enrichment analysis reveals that stemness-associated pathways are significantly enriched in the high-risk cohort. (**D**) Assessment of the influence of the TME on immunotherapy response. (**E**) IC50 analysis of targeted therapeutic agents demonstrates a significantly reduced IC50 value for AZD6244 in the high-risk group, suggesting that high-risk patients may derive greater therapeutic benefit from this treatment. (**F**) Distribution of drug categories identified through CMap analysis. (**G**) Summary of the drug screening workflow. (**H**) Scatter plots and box plots illustrating the correlation between drug AUC values and the risk score. (ns, not significant, *P < 0.05, **P < 0.01).

Figure 8. Identification of hub GSC-Related genes using machine learning approaches. (**A**) Top 100 GSC-associated genes ranked by their importance scores derived from the random forest algorithm. (**B–C**) Performance metrics of the optimized 31-gene random forest classification model. (**D**) Comparative assessment of seven classification algorithms demonstrates that the random forest model attains the highest AUC value. (**E**) Confusion matrix illustrating classification accuracy. (**F**) Decision curve analysis for evaluating clinical utility. (**G**) Performance evaluation of the random forest model on an independent validation dataset. (**H**) SHAP value analysis for enhanced model interpretability.

Figure 9. Expression and stemness verification of TUBB2B in GBM. (**A-B**) Western blot analysis demonstrated that TUBB2B was significantly upregulated in GBM tissues. (**C**) qRT-PCR showed that the mRNA level of TUBB2B was significantly elevated in GBM tissues. (**D-F**) In GSC derived from GBM, CD133 and TUBB2B show high expression. (**G-H**) IHC validation of TUBB2B expression in GBM. (**I-J**)

IF showed that TUBB2B and CD133 were simultaneously significantly upregulated in GBM tissues. (**K-M**) In GSC derived from the GBM cell lines (U87MG, U251 and T98G cell lines), CD133 and TUBB2B show high expression.

Figure 10. Verification of the therapeutic effects of shTUBB2B and temozolomide. (**A-C**) The expression changes of CD133 and OLIG2 in GSC derived from GBM treated with shTUBB2B and TMZ. (**D-F**) The expression changes of CD133 and OLIG2 in U87MG treated with shTUBB2B and TMZ. (**G-H**) CCK8 assay of GSC cells derived from GBM. (**I-J**) CCK-8 assay of GSC cells derived from U87MG. (**K-L**) Transwell assays. (**M-N**) EdU assays.

Supplementary Files

This is a list of supplementary files associated with this preprint. Click to download.

- SupplementaryTable1.xlsx
- SupplementaryTable2.xlsx
- SupplementaryTable3.xlsx
- SupplementaryTable7.xlsx
- SupplementaryTable11.xlsx
- SupplementaryTable6.xlsx
- SupplementaryTable4.xlsx
- SupplementaryTable8.xlsx
- SupplementaryTable5.xlsx
- SupplementaryTable10.xlsx
- SupplementaryTable9.xlsx
- SupplementaryFile.docx
- RawdateofWesternblot.docx